Induction of a Timed Metabolic Collapse to Overcome Cancer Chemoresistance

Nick van Gastel[1,2], Jessica B. Spinelli[3], Azeem Sharda[1,2], Amir Schajnovitz[1,2], Ninib Baryawno[1,2,4], Catherine Rhee[1,2], Toshihiko Oki[1,2], Eliane Grace[1,2], Heather J. Soled[1,2], Charles Vidoudez[5], Sunia A. Trauger[5], Marcia C. Haigis[3], David T. Scadden[1,2]*

[1]Department of Stem Cell and Regenerative Biology, Harvard Stem Cell Institute, Harvard University, Cambridge, MA 02138, USA

[2]Center for Regenerative Medicine, Massachusetts General Hospital, Boston, MA 02114, USA

[3]Department of Cell Biology, Harvard Medical School, Boston, MA 02115, USA

[4]Childhood Cancer Research Unit, Department of Women's and Children's Health, Karolinska Institutet, 17177 Stockholm, Sweden.

[5]FAS Small Molecule Mass Spectrometry Facility, Harvard University, Cambridge, MA 02138, USA

* Correspondence: david_scadden@harvard.edu

Summary

Cancer relapse begins at the moment malignant cells pass through the extreme metabolic bottleneck of stress from chemotherapy and the by-products of massive surrounding cell death. In acute myeloid leukemia (AML), complete remissions are common, but few are cured. We tracked AML cells *in vivo*, defined the moment of maximal response following chemotherapy, captured persisting cells and conducted unbiased metabolic analysis, revealing a metabolite profile distinct from the pre-chemo growth or post-chemo relapse phase. Persisting cells used glutamine in a distinctive manner, preferentially fueling pyrimidine synthesis and glutathione generation, but not oxidative phosphorylation. Notably, malignant cell pyrimidine synthesis also required aspartate provided by specific bone marrow stromal cells. Blunting glutamine metabolism or pyrimidine synthesis selected against residual cells and improved survival in AML mouse models. We propose that timed cell-intrinsic or niche-focused metabolic disruption can exploit a transient vulnerability and induce a metabolic collapse in cancer cells to overcome chemoresistance.

Keywords

acute myeloid leukemia, cell metabolism, tumor microenvironment, bone marrow niche, chemotherapy, resistance, glutamine, aspartate, pyrimidine synthesis, metabolic inhibitor

Graphical Abstract

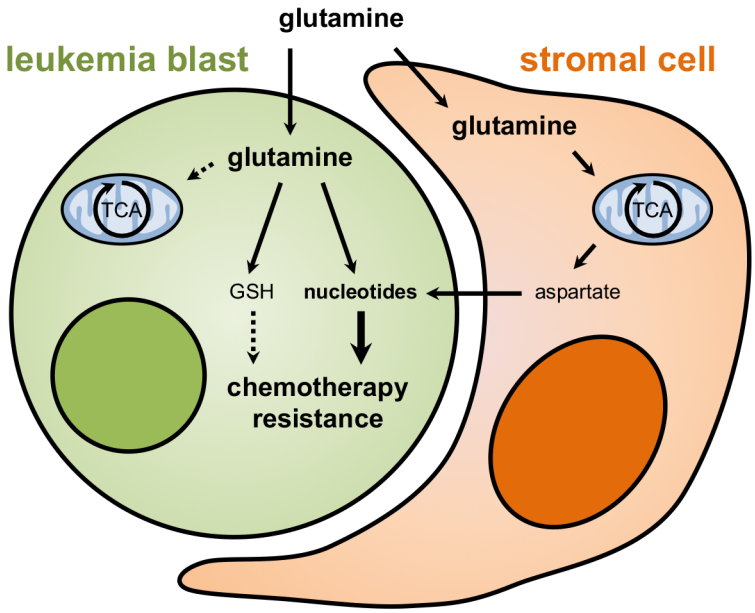

Introduction

Per evolutionary biology, when a population is subjected to a stress event or "bottleneck", only the individuals that have the ability to adapt will survive. Populations of cells behave similarly, as Peter C. Nowell proposed in 1976 to explain the clonal evolution of cancer cell populations (Nowell, 1976). Clonal evolution has been studied particularly well in acute myeloid leukemia (AML), a highly lethal hematopoietic cancer where residual founder clones persist through therapy and ultimately cause relapse (Ding et al., 2012a). Yet, genetic analysis has provided only limited insight into chemotherapy resistance commonly observed in AML, and driver mutations are frequently not amenable to targeted therapies (Magee, 2017). We and others have shown that AML cells have distinctive metabolic dependencies compared with their normal counterparts, often irrespective of the driving mutations (Chen et al., 2016, German et al., 2016, Jacque et al., 2015, Lagadinou et al., 2013, Ni et al., 2019, Pei et al., 2013, Sykes et al., 2016, Wang et al., 2014). Metabolic networks also endow cells with evolutionary-ancient stress protection systems that are independent of transcriptional changes, providing a first line defense mechanism to cope with exogenous pressure (Keller et al., 2017, Kültz, 2005, Naviaux, 2014).

We hypothesized that the stress of chemotherapy imposes an extreme metabolic bottleneck through which residual cells must pass to cause relapse. That stress state is transient, represented by the challenges of chemotherapeutic agents and cell degradation products from massive cell death in the local milieu. It will not be reflected in relapse cells at the time cancer reemergence is clinically evident, since much of the local environment and intracellular imbalances will have re-equilibrated. Rather, it can only be observed in cells extracted from the *in vivo* context where maximal cell death has occurred and chemotherapy by-products are being cleared. This transient moment of stress that drives initial leukemia regeneration has been described in patients as well as patient-derived xenografts, and is characterized by the emergence of leukemia-regenerating cells which give rise to relapse (Boyd et al., 2018, Farge et al. 2017). Defining metabolic dependencies of these residual, leukemia-regenerating

cells may reveal vulnerabilities that can be therapeutically exploited. We sought to determine whether timed, targeted perturbations can induce metabolic collapse of residual malignant cells to overcome chemoresistance.

We developed methods to track real-time changes to AML in live animals, capture cells at particular times, acquire unbiased metabolic profiles of the cells and test inferred dependencies *in vitro* and *in vivo*. We defined specific alterations in cell metabolism that allow AML cells to persist through the selection stress of chemotherapy, in part by co-opting metabolic activity of neighboring stromal cells, and show that these can be manipulated in a timed manner to improve survival from the disease.

Results

AML Cells Exhibit Transient Metabolic Changes in Response to Chemotherapy

The point of maximal metabolic stress can be functionally identified as the "point of maximal response" after chemotherapy since thereafter resistant cells have passed through the bottleneck and begun the regrowth that characterizes relapse. To determine this moment, we used a triple transgenic mouse model in which cells express MLL-AF9, driving leukemia development, as well as luciferase and GFP (Fig. S1A). We intravenously transplanted culture-expanded bone marrow cells derived from terminally ill primary mice into secondary wildtype recipients, leading to the establishment of a fast-developing disease that can be monitored through bioluminescence imaging (Fig. S1B). We treated mice with an induction chemotherapy (iCT) regimen that closely mimics the one used in the clinical care of people (cytarabine for 5 days + doxorubicin for the first 3 days) or with vehicle, followed disease progression, and discovered that the moment of maximal response occurs approximately three days after the last dose of chemotherapy (Fig. S1B-C).

We then developed a methodology to investigate the metabolic profile of freshly isolated AML cells. We isolated bone marrow cells of mice subjected to vehicle treatment (day 3 after vehicle), at the time of maximal response after iCT (day 3 after iCT), or after relapse (day 10 after iCT), sorted GFP^+ AML cells using fluorescence-activated cell sorting (FACS) and extracted polar metabolites (Fig. 1A). Samples were kept at 4°C in phosphate-buffered saline (PBS) at all times to minimize metabolic disturbance (Dietmair et al., 2010). The total time needed for cell processing and FACS sorting was 45 minutes, which was kept the same for all samples irrespective of the treatment group. We performed experiments to confirm that subjecting the cells to FACS minimally impacts their metabolite profile (Fig. S1D). The levels of intracellular metabolites in 25,000 sorted cells were then determined by untargeted metabolomics analysis using liquid chromatography-coupled tandem mass spectrometry (LC-MS/MS). We were able to measure 654 metabolites, of which 129 were identified based on their MS/MS spectra using the mzCloud database, and another 211 could be putatively identified based on their molecular

weight by searching the Human Metabolome database and KEGG Compound database (Table S1). The 340 putatively identified metabolites were then further analyzed using the MetaboAnalyst software. Principal component analysis showed that while groups clustered closely together, the iCT group separated from the vehicle and relapse groups (Fig. S1E). Statistically, 125 metabolites differed significantly between the groups (ANOVA, FDR < 0.01; Table S2), and unsupervised clustering of samples based on the 75 most significantly different metabolites revealed the specific metabolic signature of each group (Fig. 1B).

Metabolic pathway enrichment analysis using the (putatively) identified metabolites revealed the related "glutamine and glutamate metabolism" and "alanine, aspartate and glutamate metabolism" as the top pathways distinguishing iCT-treated cells from vehicle-treated and relapsed cells (Fig. 1C). Glutamine, glutamate and aspartate, central metabolites in these pathways, are low in vehicle-treated cells, high in the residual cells at the moment of maximal response to iCT, and low again after relapse (Fig. 1D), suggesting a role in the immediate stress response to chemotherapy. Tricarboxylic acid (TCA) cycle metabolites (alpha-ketoglutarate, succinate, fumarate, malate, citrate, cis-aconitate), lactate, and most other amino acids (alanine, arginine, leucine/isoleucine, methionine, phenylalanine, proline, valine) did not show similar changes (Fig. S1F). Targeted analysis of polar metabolites in the aforementioned treatment conditions corroborated the observed changes in glutamine, glutamate and aspartate (Fig. S1G). Interestingly, when AML cells from vehicle or iCT-treated mice were isolated at the moment of maximal response and cultured *in vitro* for 24 hours, the differences in glutamine, glutamate and aspartate reversed (Fig. S1H). We also did not find a difference in glutamine levels when cells were treated with iCT in culture (Fig. S1I), showing that the metabolic profile of AML cells is highly dependent on the local microenvironment.

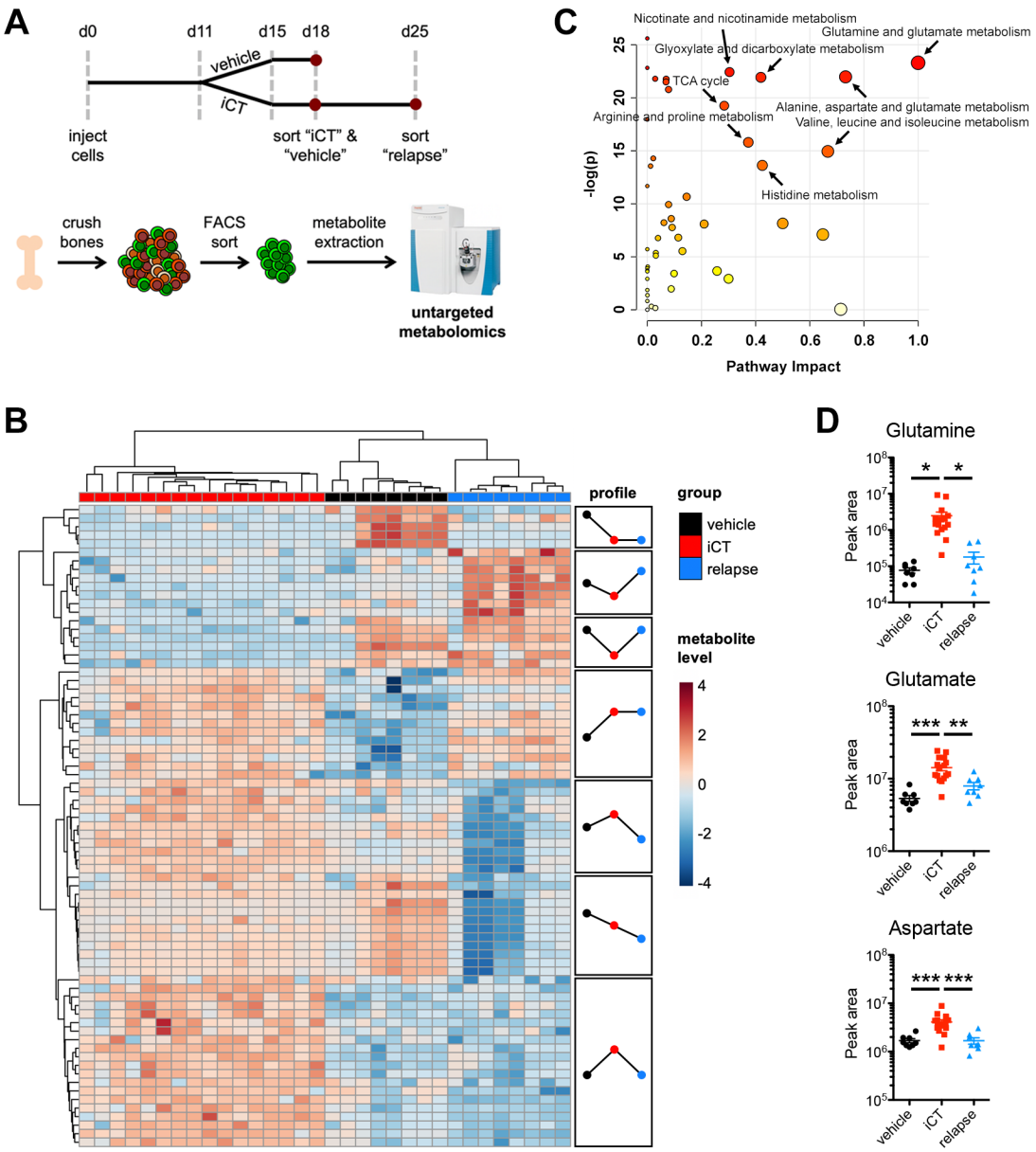

Figure 1. AML Cells Exhibit Transient Metabolic Changes in Response to Chemotherapy.

(**A**) Schematic overview of the experimental design for untargeted metabolic profiling of freshly isolated mouse MLL-AF9 AML cells. iCT: induction chemotherapy (5 days of cytarabine 100 mg/kg + 3 days of doxorubicin 3 mg/kg, I.P.). (**B**) Heatmap-based visualization of the metabolic profile of MLL-AF9 AML cells obtained from mice with vehicle treatment (vehicle group), at 3 days after induction chemotherapy (iCT group; representing the moment of maximal response) or at 10 days after iCT (relapse group). (**C**) Metabolic Pathway Enrichment Analysis using putatively identified metabolites of the iCT versus vehicle/relapse groups showing metabolic pathways enriched in MLL-AF9 AML cells at the moment of maximal response after iCT treatment. Pathway impact is a measure for the percentage of metabolites that were measured in a given pathway, as well as their relative importance in that pathway. (**D**) Levels of glutamine, glutamate and aspartate in vehicle, iCT or relapse MLL-AF9 AML cells as measured by untargeted metabolomics. Data are represented as mean ± SEM. *p<0.05, **p<0.01, ***p<0.001. See also Figure S1.

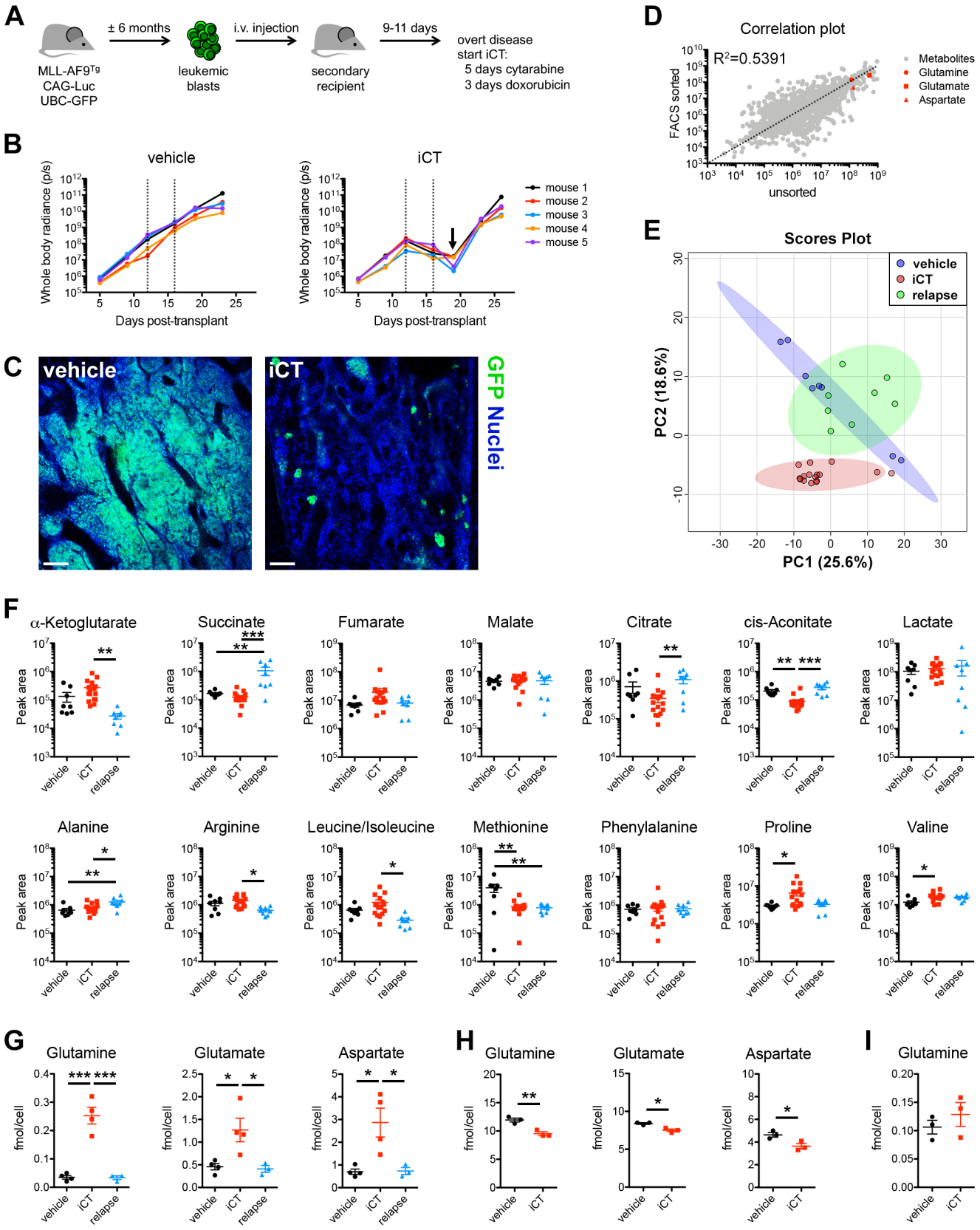

Figure S1. AML Cells Exhibit Transient Metabolic Changes in Response to Chemotherapy (related to Figure 1).

(**A**) Schematic overview of the AML mouse model used in this study. (**B**) Disease progression, visualized by bioluminescence imaging, in mice engrafted with MLL-AF9 AML cells at day 0, treated with vehicle (left) or iCT (right). Arrow indicates the moment of maximal response. (**C**) Histological visualization of GFP-expressing MLL-AF9 AML cells in the bone marrow of vehicle treated mice (left) or mice treated with iCT (right), at the moment of maximal response. (**D**) Analysis of the effect of FACS sorting on the metabolic profile of MLL-AF9 AML cells, showing correlation of individual metabolite levels between unsorted and FACS-sorted cells, obtained from *in vitro* culture. Metabolites of particular interest for this study, glutamine, glutamate and aspartate, are highlighted. (**E**) Principal component analysis of metabolomics data of MLL-AF9 AML cells comparing vehicle, iCT and relapse groups. (**F**) Levels of individual metabolites in vehicle, iCT or relapse MLL-AF9 AML cells as measured by untargeted metabolomics. (**G**) Liquid chromatography-mass spectrometry (LC-MS)-based quantification of glutamine, glutamate and aspartate in vehicle, iCT or relapse MLL-AF9 AML cells. (**H**) LC-MS-based quantification of glutamine, glutamate and aspartate in vehicle- or iCT-treated MLL-AF9 AML cells isolated at the moment of maximal response and cultured *in vitro* for 24 hours. (**I**) LC-MS-based quantification of glutamine in *in vitro* cultured MLL-AF9 AML cells treated with vehicle or with 30nM cytarabine and 10nM doxorubicin (iCT) for 24 hours. Data are represented as mean ± SEM. *p<0.05, **p<0.01, ***p<0.001.

Timed Inhibition of Glutamine Metabolism Overcomes Chemoresistance in AML

To determine whether the observed increase in glutamine metabolism-associated metabolites causes chemoresistance, we assessed whether residual AML cells would be more susceptible to broad inhibition of glutamine metabolism using 6-diazo-5-oxo-L-norleucine (DON), a glutamine analog and antagonist that inhibits all glutamine-dependent enzymes (Lemberg et al., 2018). When DON was given for 5 days at the same time as iCT, no difference in survival was seen (Fig. 2A). However, when DON treatment was started after completion of the iCT regimen and covered the moment of maximal response, either daily for a short time (Fig. 2B) or continuously every other day (Fig. 2C), we observed a clear survival benefit. Short term treatment with DON after iCT improved elimination of AML cells (Fig. 2D,E), and increased double stranded DNA breaks in residual cells (Fig. 2F). Treatment of mice with DON lead to accumulation of glutamine in AML cells while partially reducing the increase in glutamate induced by iCT treatment, showing that DON effectively inhibits glutamine metabolism in AML cells (Fig. S2). Interestingly, aspartate levels did not follow a similar profile as glutamate, and remained high in mice treated with iCT followed by DON (Fig. S2). We confirmed the effect of DON on residual cells in a different mouse model of AML, driven by retroviral HoxA9/Meis1 overexpression, which also showed

improved mouse survival when treated with DON after completion of the iCT regimen (Fig. 2G). These data show that activation of glutamine metabolism protects AML cells at the moment of maximal stress after chemotherapy and reveal the potential of timed inhibition of glutamine metabolism to eliminate persisting AML cells.

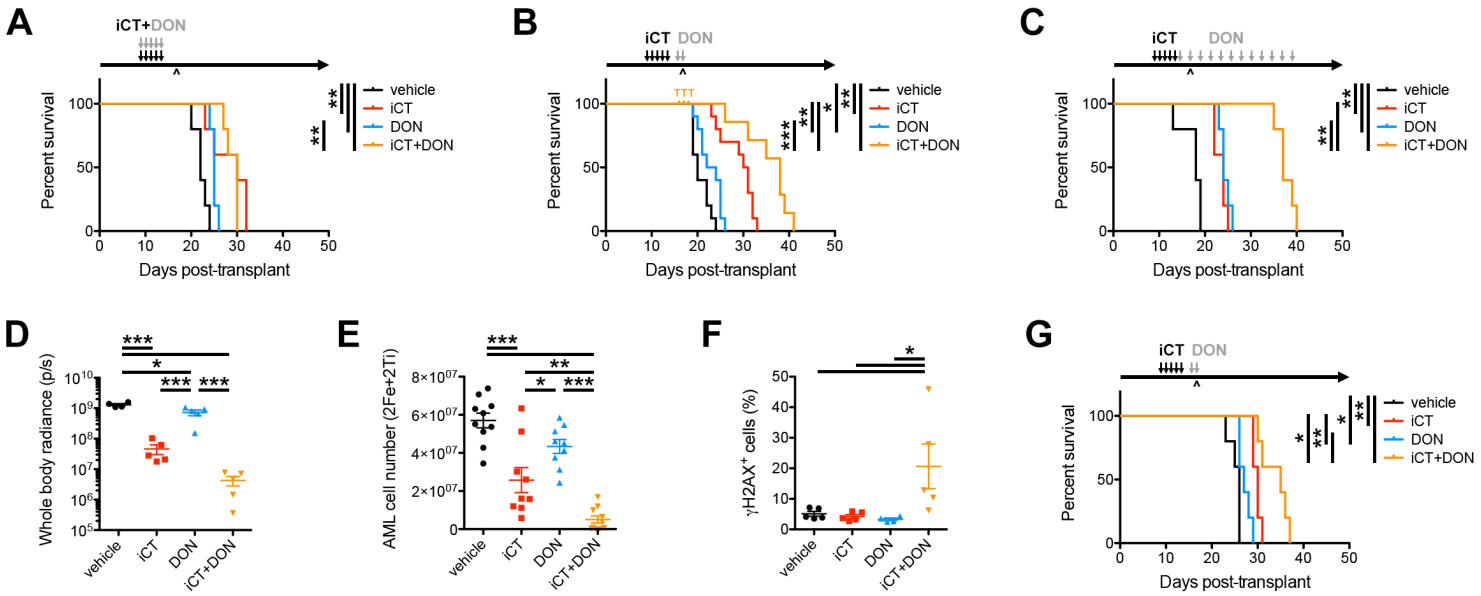

Figure 2. Timed Inhibition of Glutamine Metabolism Overcomes Chemoresistance in AML.

(**A**-**C**) Kaplan-Meier survival curves of MLL-AF9 AML-bearing mice treated with iCT and/or 6-diazo-5-oxo-L-norleucine (DON; 0.3 mg/kg, I.P.) concomitantly (A) or sequentially (B,C). For sequential treatments, mice were either treated with two doses of DON specifically targeting the moment of maximal response (B), or continuously with DON every other day following iCT (C). T: death due to drug toxicity, ^: moment of maximal response. (**D**,**E**) Disease burden of MLL-AF9 AML-bearing mice treated sequentially with iCT and/or DON (regimen as in B), determined one day after the last dose of DON through bioluminescence imaging (D) or flow cytometry (E). (**F**) Double-stranded DNA breaks in MLL-AF9 AML cells of mice treated sequentially with iCT and/or DON (regimen as in B), determined one day after the last dose of DON through flow cytometry for gamma-H2AX. (**G**) Kaplan-Meier survival curves of HoxA9/Meis1 AML-bearing mice treated sequentially with iCT and/or two doses of DON (0.3 mg/kg, I.P.) specifically targeting the moment of maximal response. Data are represented as mean ± SEM. *p<0.05, **p<0.01, ***p<0.001. See also Figure S2.

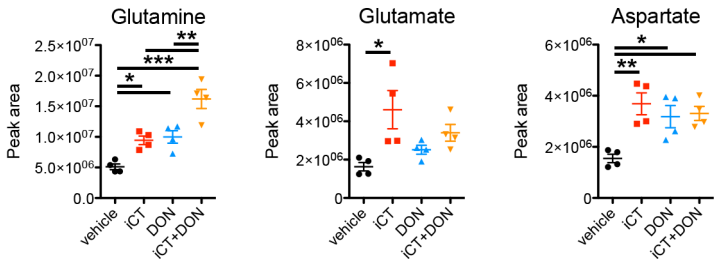

Figure S2. Timed Inhibition of Glutamine Metabolism Overcomes Chemoresistance in AML (related to Figure 2).

LC-MS-based quantification of glutamine, glutamate and aspartate in MLL-AF9 AML cells of mice treated sequentially with iCT and/or DON (regimen as in Figure 2B), determined one day after the last dose of DON. Data are represented as mean ± SEM. *p<0.05, **p<0.01, ***p<0.001.

Residual AML Cells Do Not Depend on Glutaminase

While DON has been tested in Phase I and II clinical trials for both solid tumors and leukemia in the 1980s, it was abandoned due to limited efficacy as a single agent and the occurrence of dose-dependent side effects including nausea, vomiting and mucositis (Lemberg et al., 2018). Due to these toxicity issues (Fig. 2B), we sought alternative glutamine pathway inhibitors. The enzyme glutaminase (GLS) has been shown to be a metabolic vulnerability in AML (Gregory et al., 2019, Jacque et al., 2015, Matre et al., 2016), but whether it mitigates the metabolic stress following chemotherapy is unknown. We first confirmed that genetic or pharmacological inhibition of GLS reduced AML cell viability *in vitro* (Fig. S3A-C), in line with previous studies. Unexpectedly, GLS knockdown had no effect on disease progression or response to iCT *in vivo* (Fig. 3A). In addition, treatment of mice with a GLS inhibitor during a short window at the moment of maximal response after iCT did not enhance AML cell elimination or mouse survival (Fig. 3B). These results again highlight that cellular metabolism and metabolic dependencies are microenvironment dependent, and further show that AML cells persisting after chemotherapy, while critically depending on glutamine metabolism, do not require the enzyme glutaminase for their survival.

To better understand the metabolic fate of glutamine in residual AML cells, the comparative transcriptomic profiles of vehicle- and iCT-treated AML cells at the moment of maximal response were analyzed. The expression levels of most enzymes that metabolize glutamine or glutamate were unchanged in persisting cells (Fig. 3C). While some individual enzymes showed increased expression post chemotherapy, no single pathway stood out as particularly altered (Fig. 3C). In accordance, gene set enrichment analysis comparing vehicle- and iCT-treated cells did not return any glutamine-related pathways amongst the top hits (Fig. 3D, Fig. S3D). In contrast, several other metabolic pathways were found to be highly enriched in residual AML cells at the transcriptomic level, including the reactive oxygen species (ROS) pathway, fatty acid metabolism, oxidative phosphorylation, glycolysis and cholesterol metabolism (Fig. 3D, Fig. S3E). A recent study has shown that persisting human AML cells require oxidative metabolism fueled by fatty acid oxidation, and display high levels of reactive oxygen species and an increased mitochondrial activity (Farge et al. 2017). We made similar observations in our mouse model of MLL-AF9 AML, with residual cells showing a higher mitochondrial membrane potential and increased ROS levels (Fig. 3E,F), thus confirming previous findings.

Closer examination of glutamine metabolism-related genes revealed increased expression of several glutamine transporters, including *Slc1a5*, *Slc38a1*, *Slc7a5* and *Slc7a6*, in residual AML cells (Fig. 3C). Flow cytometric analysis confirmed a transient increase in SLC38A1 protein levels after chemotherapy. This was not seen in normal hematopoietic stem and progenitor cell populations (Fig. 3G), suggesting that the changes in glutamine metabolism in response to chemotherapy are specific for AML cells. We also analyzed two publicly available human AML survival datasets, and found that high expression of *SLC38A1* strongly associates with poor overall survival in both datasets (Fig. 3H), which was not found for other glutamine metabolism-related genes (Fig. S3F). Together, these data show that the transient increase in glutamine metabolism in residual AML cells seen at the metabolite level is not reflected at the mRNA level. The single exception is that of glutamine transporters.

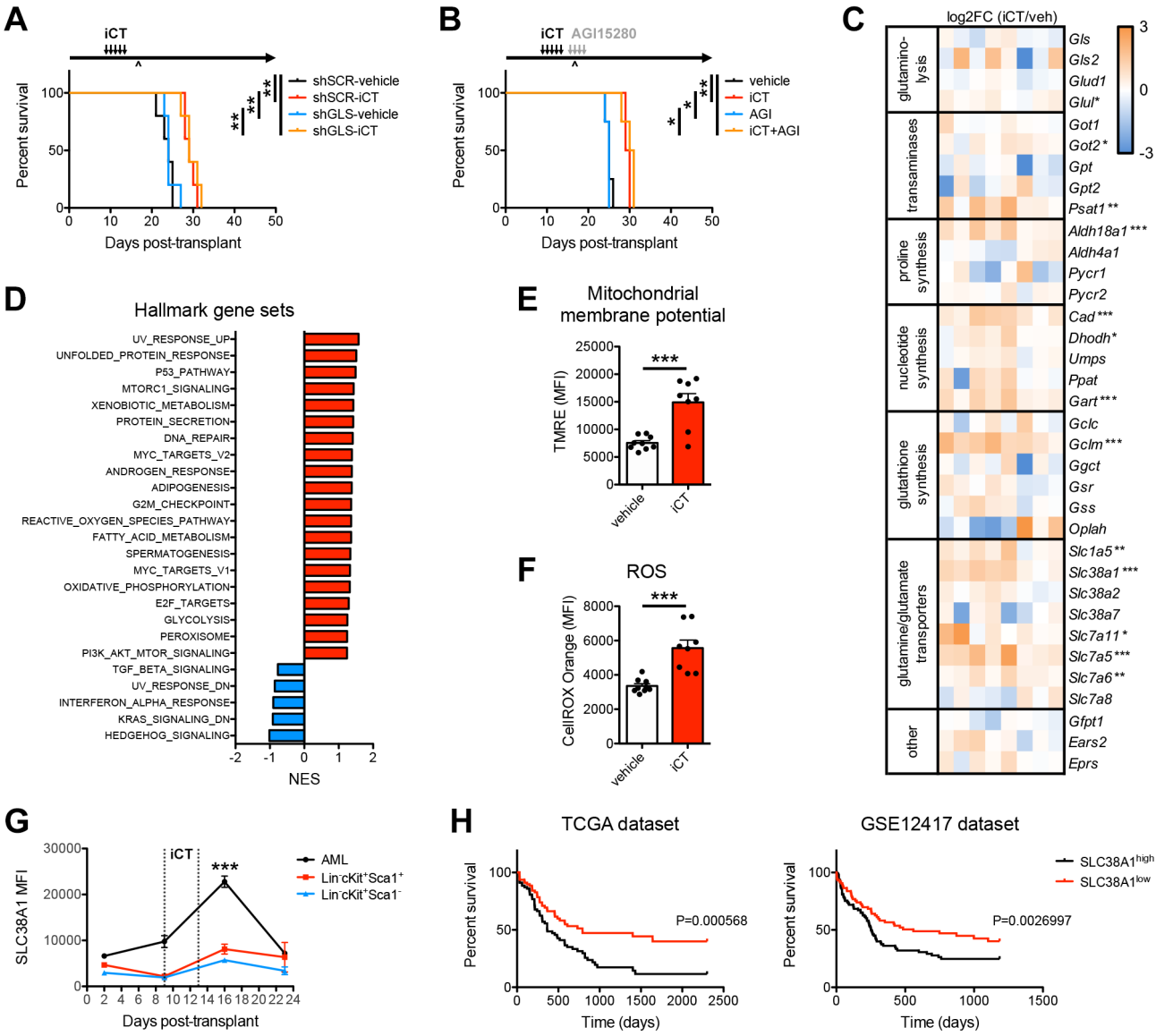

Figure 3. Residual AML Cells Do Not Depend on Glutaminase.

(**A**) Kaplan-Meier survival curve of mice engrafted with MLL-AF9 AML cells transduced with scrambled short hairpin RNA (shSCR) or shRNA targeting glutaminase (shGLS), treated with or without iCT. (**B**) Kaplan-Meier survival curves of MLL-AF9 AML-bearing mice treated sequentially with iCT and/or four days of AGI15280 (150 mg/kg twice daily, P.O.) specifically targeting the moment of maximal response. ^: moment of maximal response. (**C**) Heatmap of RNA sequencing data comparing expression of genes related to glutamine metabolism in MLL-AF9 AML cells obtained from mice treated with vehicle or chemotherapy, at the moment of maximal response. (**D**) Gene set enrichment analysis (Hallmark gene sets) in iCT- versus vehicle-treated MLL-AF9 AML cells obtained at the moment of maximal response. NES: normalized enrichment score. (**E**,**F**) Mitochondrial membrane potential as measured by tetramethylrhodamine ethyl ester (TMRE) staining (E) and levels of reactive oxygen species (ROS) as measured by CellROX Orange staining (F) in MLL-AF9 AML cells obtained from mice treated with vehicle or chemotherapy, at the moment of maximal response. (**G**) Flow cytometric analysis of SLC38A1 protein levels on the surface of MLL-AF9 AML cells and on Lin$^-$cKit$^+$Sca1$^+$ and Lin$^-$cKit$^+$Sca1$^-$ normal hematopoietic stem

and progenitor cells, at different times during the course of iCT treatment. (**H**) Kaplan-Meier survival curves of AML patients grouped according to expression of SLC38A1 above or below the median. Data were obtained from the TCGA dataset or the GSE12417 dataset. Data are represented as mean ± SEM. *p<0.05, **p<0.01, ***p<0.001. See also Figure S3.

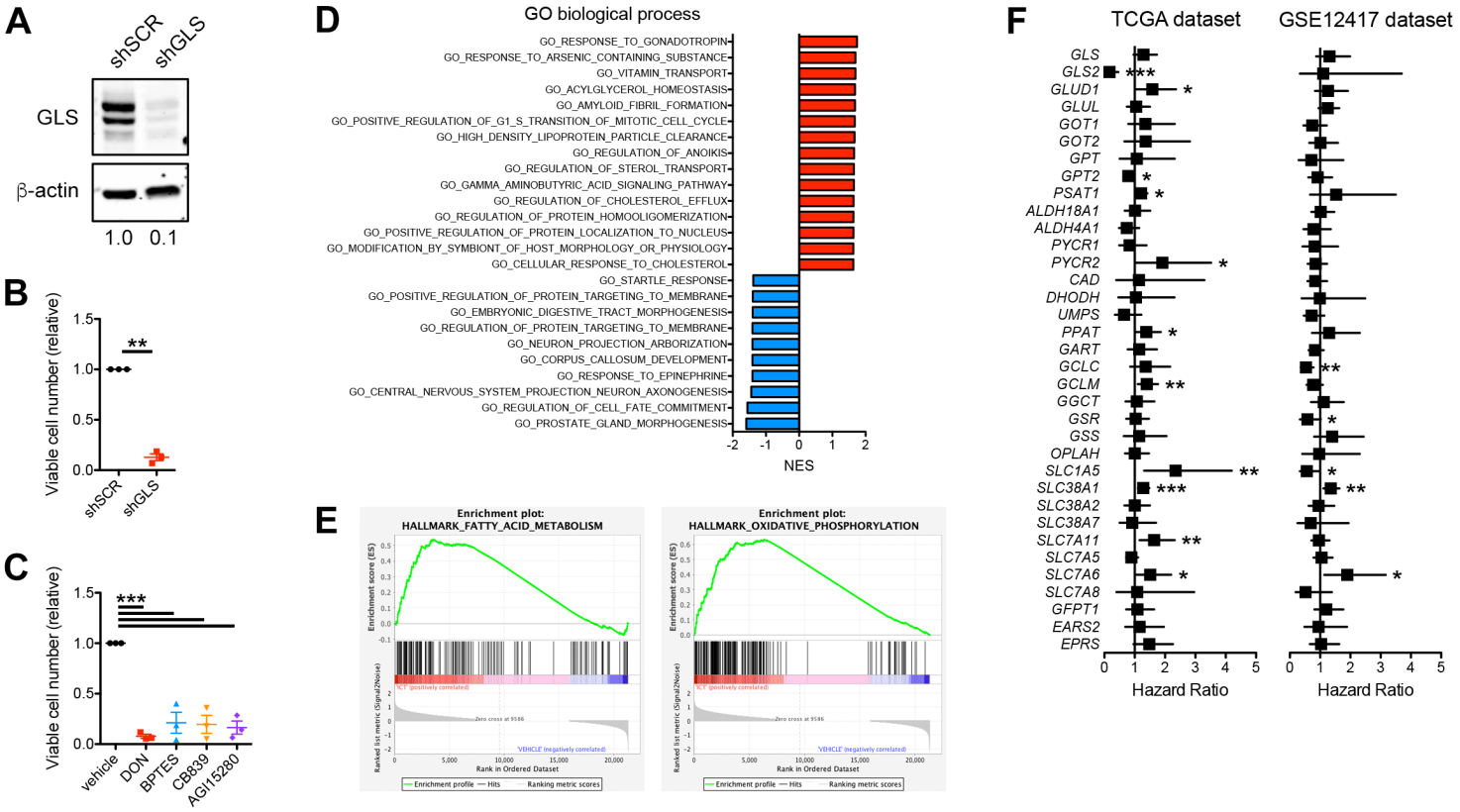

Figure S3. Residual AML Cells Do Not Depend on Glutaminase (related to Figure 3).

(**A**) Immunoblot detection of GLS in MLL-AF9 cells transduced with shSCR or shGLS, with β-actin as loading control. (**B**) Relative number of viable MLL-AF9 AML cells obtained 72 hours after transduction of cells with shSCR or shGLS. (**C**) Relative number of viable MLL-AF9 AML cells obtained 72 hours after treatment of cells with the pan-glutamine metabolism inhibitor DON (1 μM) or the GLS inhibitors BPTES (5 μM), CB839 (0.5 μM) or AGI15280 (0.5 μM). (**D**) Gene set enrichment analysis (gene ontology biological process gene sets) in iCT- versus vehicle-treated MLL-AF9 AML cells obtained at the moment of maximal response. NES: normalized enrichment score. (**E**) Enrichment plots for genes related to fatty acid metabolism (left) and oxidative phosphorylation (right) comparing iCT- and vehicle-treated MLL-AF9 AML cells obtained at the moment of maximal response. (**F**) Hazard ratios for AML patient survival, bifurcated according to median expression of genes related to glutamine metabolism, in the TCGA and GSE12417 datasets. Data are represented as mean ± SEM (B,C) or as Hazard Ratio ± 95% confidence intervals (F). *p<0.05, **p<0.01, ***p<0.001.

Glutamine Metabolism Drives AML Chemoresistance by Fueling Pyrimidine Synthesis

To assess the metabolic fate of glutamine in residual AML cells, *in vivo* stable isotope tracing was performed. Bolus intravenous injection of $^{13}C_5$-glutamine lead to rapid glutamine pool labeling in the peripheral blood and bone marrow plasma, maintained at 45-55% labeling for 10 minutes, after which it declined (Fig. S4A). Labeling of glutamine in AML cells occurred slower with only 21% of the pool labeled at 10 minutes, and a rapid decline thereafter. Based on these results, we chose the 10 minutes time point for analyses. Notably, bolus infusion revealed labeling of glutamine and glutamate pools in AML cells, but strikingly minimal labeling of the TCA cycle intermediates alpha-ketoglutarate and succinate (Fig. S4A,B). To validate that our LC-MS techniques were capable of detecting glutamine-derived carbon incorporation into the TCA cycle, we profiled metabolites in the liver of the same mice that were utilized for the AML experiments. The liver showed extensive conversion of glutamine into TCA cycle metabolites including alpha-ketoglutarate and succinate, in line with the expected pattern for cells using glutamine to fuel the TCA cycle (Fig. S4C) (Häussinger and Schliess, 2007). This shows that in contrast to previous reports describing glutamine contribution to the TCA cycle *in vitro* in AML cells (Gregory et al., 2019, Matre et al., 2016), *in vivo* this does not seem to be a predominant fate of glutamine. These results mirror previous findings in mouse models of lung cancer, where similar discrepancies between *in vitro* and *in vivo* glutamine metabolism have been described (Davidson et al., 2016).

To understand how residual AML cells utilize glutamine, we then injected $^{13}C_5$-glutamine or $^{15}N_2$-glutamine intravenously into vehicle- and iCT-treated mice at the moment of maximal response. Analysis of labeling patterns in AML cells showed no changes in the contribution of glutamine-derived carbon or nitrogen to amino acids or TCA cycle metabolites (Fig. 4A,B). Rather, a substantial increase of glutamine carbon and nitrogen incorporation into glutathione was observed (Fig. 4C). In addition, glutamine nitrogen incorporation into nucleotides was markedly elevated (Fig. 4D), especially into the pyrimidine uridine 5'-monophosphate (UMP). UMP gets one nitrogen from glutamine and one from aspartate, which is synthetized from glutamine-derived glutamate through transaminase activity (Fig.

297 S4D). We observed increased fractions of UMP both containing one or two labeled nitrogen atoms,
298 showing that residual AML cells fuel pyrimidine synthesis with glutamine nitrogen both directly and
299 indirectly through aspartate. Investigation of metabolite pool sizes revealed decreased levels of reduced
300 glutathione (GSH) and unchanged levels of oxidized glutathione (GSSG) in residual cells (Fig. 4E).
301 Together with the tracing results (Fig. 4C), this suggests that residual AML cells ramp up glutathione
302 synthesis to replenish depleted GSH pools. Absolute levels of UMP in contrast were increased in
303 residual cells (Fig. 4F), in line with increased pyrimidine synthesis fueled by glutamine. AML cells
304 persisting after chemotherapy thus require glutamine-derived carbon and nitrogen to fuel glutathione
305 synthesis and glutamine nitrogen to generate high levels of pyrimidine nucleotides.
306
307 Next, we investigated the potential of targeting glutathione synthesis and nucleotide synthesis
308 individually to eliminate residual AML cells. To inhibit glutathione biosynthesis, we used the compound
309 L-buthionine-sulfoximine (BSO), which inhibits glutamate-cysteine ligase (GCL). Treatment of AML-
310 bearing mice with BSO for 4 days following iCT showed no difference in survival compared to iCT alone
311 (Fig. 4G). We then blocked pyrimidine synthesis using brequinar (BRQ), which inhibits the enzyme
312 dihydroorotate dehydrogenase (DHODH) (Fig. S4D). Administration of only two doses of BRQ following
313 iCT was sufficient to significantly extend survival of AML-bearing mice compared to iCT treatment alone
314 (Fig. 4G, Fig. S4E). Similar to the effects of DON, short term treatment with BRQ after iCT improved
315 elimination of AML cells from the bone marrow (Fig. S4F). These data show that residual AML cells
316 require glutamine-dependent pyrimidine synthesis for their survival, while glutathione synthesis is not
317 essential. In line with these findings, we found that the pan-glutamine metabolism inhibitor DON
318 prevented the increase of UMP levels in residual AML cells (Fig. S4G), confirming that these cells
319 require glutamine to synthesize pyrimidines.
320
321 To test whether our metabolic targeting strategies effectively eliminate leukemia-initiating cells (Krivtsov
322 et al., 2006), we next analyzed expression of the immature cell markers CD34 and cKit and tested the
323 colony-forming ability of AML cells obtained from mice treated with vehicle or iCT, alone or in

combination with DON or BRQ (Figure 4H,I). Treatment with iCT alone increased the percentage of $CD34^+cKit^+$ cells as well as the number of colony-forming units (CFUs), while DON alone had no effect on marker expression but moderately increased the number of CFUs compared to vehicle-treated mice, indicating that these strategies eliminate bulk AML cells but relatively spare leukemia-initiating cells. The combination of iCT and DON normalized both the percentage of $CD34^+cKit^+$ cells as well as the number of CFUs back to vehicle levels, showing that iCT sensitizes both bulk AML cells and leukemia-initiating cells to DON treatment. BRQ, in line with its pro-differentiation effect on AML cells (Sykes et al., 2016), strongly reduced the percentage of $CD34^+cKit^+$ cells as well as the number of CFUs. The combination of iCT and BRQ had similar effects on the percentage of $CD34^+cKit^+$ cells compared to BRQ alone, but further reduced the percentage of $CD34^-cKit^+$ cells and the number of CFUs. Together, these data show that leukemia-initiating cells persisting after chemotherapy are effectively targeted by inhibitors of glutamine metabolism or pyrimidine synthesis.

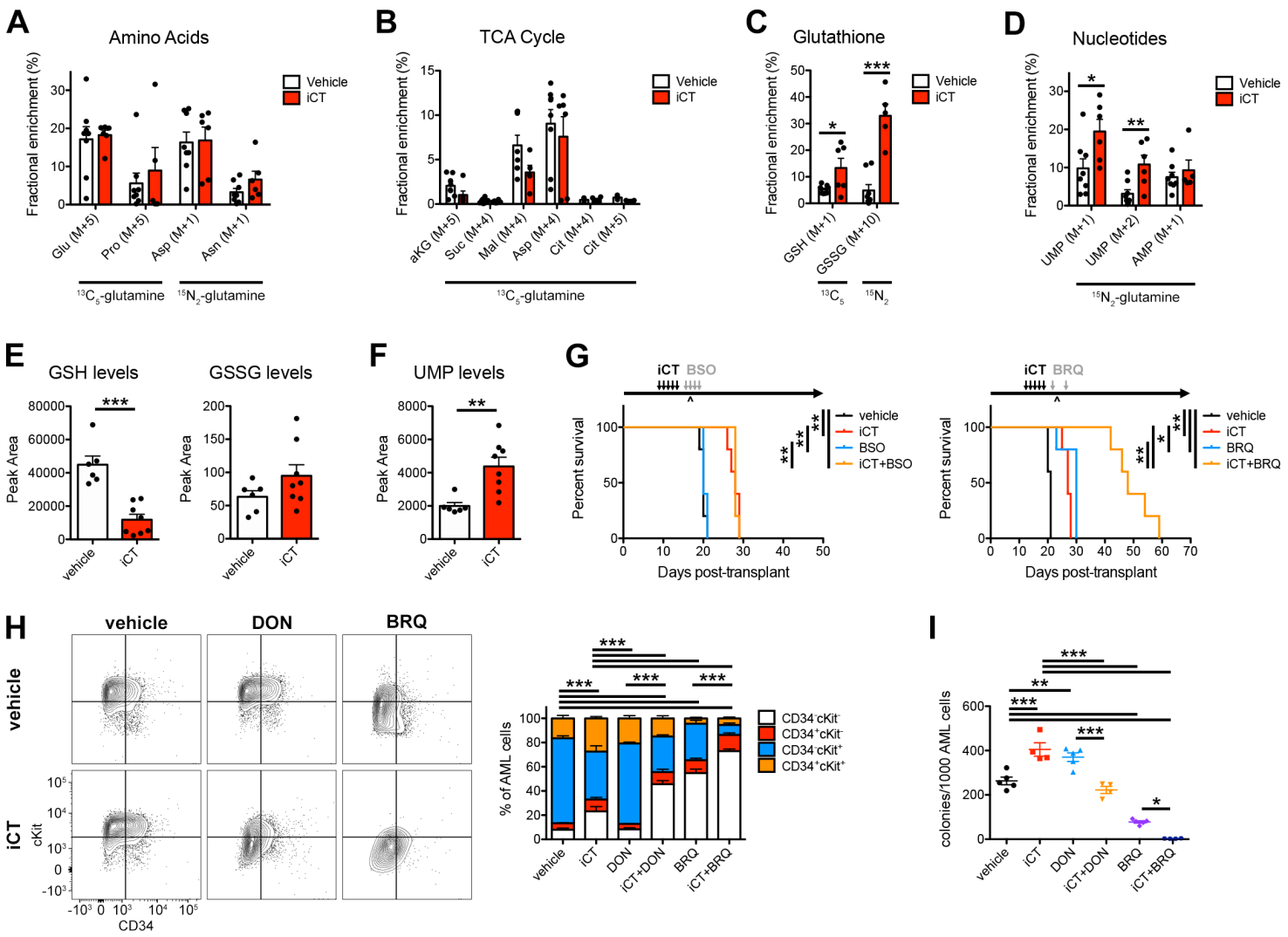

Figure 4. Glutamine Metabolism Drives AML Chemoresistance by Fueling Pyrimidine Synthesis.

(**A**-**D**). Contribution of glutamine carbon and nitrogen to amino acids (A), metabolites involved in the TCA cycle (B), glutathione (C) and nucleotides (D) in MLL-AF9 AML cells obtained from vehicle- and iCT-treated mice at the moment of maximal response. Glu: glutamate, Pro: proline, Asp: aspartate, Asn: asparagine, aKG: alpha-ketoglutarate, Suc: succinate, Mal: malate, Cit: citrate, GSH: reduced glutathione, GSSG: oxidized glutathione, UMP: uridine 5'-monophosphate, AMP: adenosine 5'-monophosphate. (**E**,**F**) Levels of GSH and GSSG (E) or UMP (F) in MLL-AF9 AML cells obtained from vehicle- and iCT-treated mice at the moment of maximal response. (**G**) Kaplan-Meier survival curves of MLL-AF9 AML-bearing mice treated sequentially with iCT and/or L-buthionine-sulfoximine (BSO, 2.23 mg/kg twice daily, I.P. + 4.45 mg/ml in drinking water; left) or brequinar (BRQ, 50 mg/kg, I.P.; right). ^: moment of maximal response. (**H**,**I**) Flow cytometric visualization and quantification of CD34 and cKit levels (H) and colony-forming capacity (I) in AML cells obtained from mice sequentially treated with iCT and/or DON (regimen as in Figure 2B) or BRQ (regimen as in G), determined four days after the last dose of iCT. Data are represented as mean ± SEM. *p<0.05, **p<0.01, ***p<0.001. See also Figure S4.

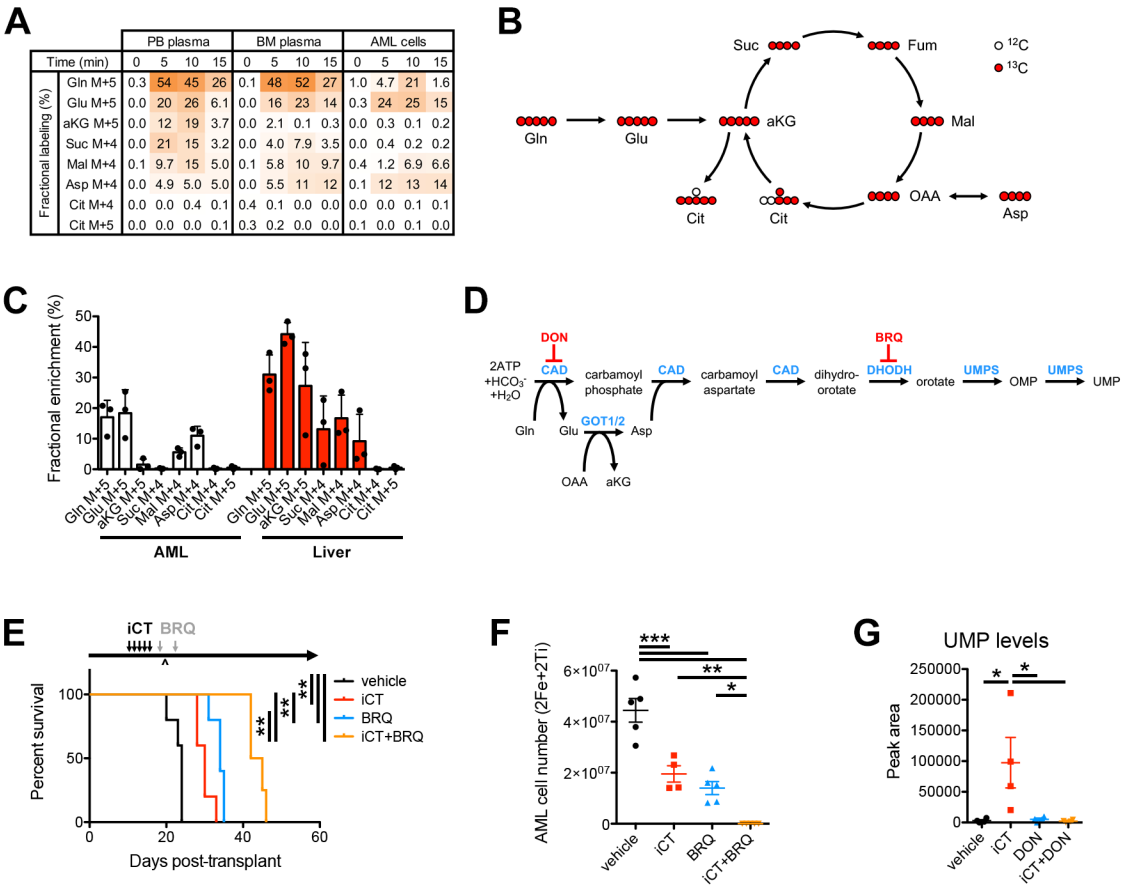

Figure S4. Glutamine Metabolism Drives AML Chemoresistance by Fueling Pyrimidine Synthesis (related to Figure 4).

(**A**) Time course of ^{13}C labeling of glutamine metabolism and TCA cycle metabolites in peripheral blood (PB) plasma, bone marrow (BM) plasma and MLL-AF9 AML cells after a bolus tail vein injection of 10.86 mg $^{13}C_5$-glutamine. (**B**) Schematic overview of expected labeling patterns from $^{13}C_5$-glutamine. White labels: ^{12}C, red labels: ^{13}C. (**C**) Labeling pattern of glutamine metabolism and TCA cycle metabolites in MLL-AF9 AML cells versus liver tissue by $^{13}C_5$-glutamine *in vivo*. (**D**) Schematic overview of the first steps of pyrimidine synthesis, indicating enzymes in blue and metabolic inhibitors in red. ATP: adenosine 5'-triphosphate, BRQ: brequinar, CAD: carbamoyl-phosphate synthetase 2/aspartate transcarbamylase/dihydroorotase, DHODH: dihydroorotate dehydrogenase, GOT: glutamate-oxaloacetate transaminase, OAA: oxaloacetate, OMP: orotidine 5'-monophosphate, UMPS: uridine 5'-monophosphate synthetase. (**E**) Kaplan-Meier survival curves of HoxA9/Meis1 AML-bearing mice treated sequentially with iCT and/or brequinar (BRQ, 50 mg/kg, I.P.; right). ^: moment of maximal response. (**F**) Flow cytometric analysis of disease burden of MLL-AF9 AML-bearing mice treated sequentially with iCT and/or BRQ (regimen as in Figure 4G), determined four days after the last dose of iCT. (**G**) LC-MS-based quantification of UMP in MLL-AF9 AML cells of mice treated sequentially with iCT and/or DON (regimen as in Figure 2B), determined one day after the last dose of DON. Data are represented as mean ± SEM. *p<0.05, **p<0.01, ***p<0.001.

Bone Marrow Stromal Cell-Derived Aspartate Supports Pyrimidine Synthesis in AML Cells

Our *in vivo* $^{13}C_5$-glutamine tracing experiments showed that AML cells have substantially different labeling patterns compared to the liver (Fig. S4C). While in liver the TCA cycle is fueled by glutamine, as demonstrated by labeling of TCA cycle intermediates by $^{13}C_5$-glutamine, AML cells show hardly any labeling of alpha-ketoglutarate, succinate and citrate, but substantial labeling of the malate and especially aspartate pools. Since aspartate is another metabolite essential for pyrimidine synthesis, we further explored the origins of this particular labeling pattern. We performed metabolic tracing using $^{13}C_5$-glutamine in MLL-AF9- and HoxA9/Meis1-driven AML lines *in vivo* and *in vitro*. Interestingly, both AML models showed the unique labeling patterns only *in vivo*, while *in vitro* they exhibited the same labeling pattern as observed in the liver samples *in vivo* (Fig. 5A). Longer *in vitro* labeling increased overall tracer enrichment, but did not change the labeling patterns (Fig. S5A). These results show that the $^{13}C_5$-glutamine labeling pattern seen in AML cells *in vivo* is not due to technical issues such as labeling time or the cell model used, but reflects a unique metabolic program of AML cells *in vivo*.

Glutamine carbon cannot end up in aspartate without going through either alpha-ketoglutarate and succinate (oxidative glutamine catabolism) or citrate (reductive carboxylation) in the TCA cycle (Fig. S4B). One possibility is that the interconversion of glutamate to aspartate occurs so rapid that labeling in the intermediates is not seen. However, further analysis of our *in vivo* $^{13}C_5$-glutamine tracing experiments revealed that labeling of glutamate and aspartate pools reached its peak in AML cells before labeling of glutamine pools (Fig. S4A). We also found that AML cells *in vivo* have very small pools of alpha-ketoglutarate, succinate and malate compared to glutamate and aspartate (Fig. S5B), making it unlikely to not see substantial labeling of these metabolites even if the interconversion rates are high. Our data thus suggest that AML cells *in vivo* obtain (glutamine-derived) aspartate from another source. Analysis of amino acid levels in peripheral blood revealed that aspartate is the lowest of all amino acids in the circulation (Fig. 5B), in accordance with previous reports (Cantor et al., 2017, Tardito et al., 2015). However, when we compared amino acid levels in the bone marrow plasma to those in the peripheral blood plasma we found that while most amino acids do not differ substantially, aspartate

levels are 70-fold higher, making it the second most abundant amino acid in bone marrow plasma (Fig. 5B). Glutamate, also of low abundance in peripheral blood, was 23-fold higher in bone marrow, while glutamine levels were 30 percent lower. Interestingly, in mice engrafted with AML cells, aspartate levels were further increased in the bone marrow plasma, while after iCT treatment aspartate levels were significantly lower (Fig. S5C). Glutamate levels followed a similar trend, while glutamine concentrations showed the opposite profile. These data suggest that AML cells may obtain aspartate from a local bone marrow source, which may be of particular importance after iCT given the increased levels of aspartate in residual AML cells (Fig. 1E) and the necessity of this metabolite for pyrimidine synthesis.

To identify the bone marrow cells responsible for local aspartate secretion, we analyzed expression of genes encoding enzymes involved in glutamine-to-aspartate conversion and for aspartate transporters in a single cell RNA sequencing dataset of the mouse bone marrow stroma that we recently generated (Fig. S5D) (Baryawno et al., 2019). Most enzymes involved in aspartate synthesis from glutamine, including *Gls*, glutamate-oxaloacetate transaminase 1 (*Got1*), *Got2* and glutamate dehydrogenase (*Glud1*), were expressed throughout the bone marrow stroma, including in Leptin Receptor $(LepR)^+CXCL12^+$ mesenchymal stromal cells (cluster 1), $S100A4^+$ fibroblasts (clusters 3, 5, 9, 15, 16), $CD31^+$ endothelial cells (clusters 0, 6, 11), $osteocalcin^+$ osteolineage cells (clusters 7, 8), $aggrecan^+$ chondrocytes (2, 4, 10, 13, 17) and $Nestin^+NG2^+$ pericytes (cluster 12) (Fig. S5E). In contrast, the aspartate/glutamate transporter *Slc1a3* was expressed almost exclusively in a subpopulation of the $LepR^+$ mesenchymal stromal cells (Fig. S5E), which we confirmed at the protein level (Fig. 5C). The presence of AML cells increased SLC1A3 levels in stromal cells and particularly in $LepR^+$ cells. In contrast, iCT treatment reduced SLC1A3 levels in $LepR^+$ cells, although they remained significantly higher compared to control mice without AML (Fig. 5D). The presence of AML cells also increased the levels of the aspartate transaminases, GOT1 and particularly GOT2, in $LepR^+$ cells (Fig. 5E). These data are consistent with AML cells inducing bone marrow stromal cells (BMSCs) to alter their metabolism to increase aspartate production and secretion.

A possible exchange of aspartate between BMSCs and AML cells was tested by *in vitro* co-culture. In line with previous studies (Behrmann et al., 2018), we found that the presence of BMSCs strikingly protected AML cells from iCT treatment (Fig. S5F). Of note, we observed an increase in glutamine levels in AML cells exposed to iCT in co-cultures (Fig. S5G). This was not seen in AML mono-cultures (Fig. S1I), but does mirror the *in vivo* response of AML cells to iCT (Fig. 1D, Fig. S1G). This shows that the presence of stromal cells better mimics the *in vivo* metabolic microenvironment of AML cells.

We then performed $^{13}C_5$-glutamine tracing experiments where stromal cells were labelled for 24 hours before washing away the tracer and adding AML cells in medium containing unlabeled glutamine. 24 hours later AML cells were sorted and stable isotope labeling patterns analyzed. BMSCs metabolized glutamine in the TCA cycle, and synthetized aspartate using glutamine carbons with ~15% of the aspartate pool fully labeled (Fig. 5F). At least part of this aspartate was then transferred to the AML cells, as evident by 11% of their aspartate pool being labeled. These data confirm the metabolic crosstalk between BMSCs and AML cells. Interestingly, AML cells also showed uptake of labeled glutamate produced by BMSCs, the only other amino acid enriched in the bone marrow plasma (Fig. 5B, Fig. S5C), highly abundant in AML cells *in vivo* (Fig. S5B) and increased after iCT treatment (Fig. 1D, Fig. S1G). We analyzed the importance of the aspartate exchange by knocking down GOT1 or GOT2 in BMSCs (Fig. S5H). Loss of GOT2 in BMSCs partially sensitized AML cells to iCT treatment, confirming that aspartate exchange contributes to the chemoprotective effect of BMSCs on AML cells (Fig. 5G). Together, these data show that BMSCs convert glutamine to aspartate, which is then transferred to AML cells enabling them to survive iCT exposure.

Since aspartate is an essential metabolite for pyrimidine synthesis, we looked for evidence in our *in vivo* tracing data that glutamine-derived aspartate is used by residual AML cells to fuel UMP synthesis. Our $^{15}N_2$-glutamine tracing data showed that both single and double ^{15}N-labeled UMP was increased in residual AML cells (Fig. 4D). Since pyrimidines get one nitrogen each from glutamine and aspartate (Fig. 5H), this suggests that the glutamine-derived aspartate provided by the BMSCs is indeed used to

support increased pyrimidine synthesis. To further confirm this, we looked for UMP containing three ^{13}C atoms in the $^{13}C_5$-glutamine *in vivo* tracing data, since aspartate, but not glutamine, contributes three carbons to UMP. We indeed found increased pools of $^{13}C_3$-UMP in residual AML cells (Fig. 5H), further supporting the concept that glutamine fuels pyrimidine synthesis in AML cells persisting after chemotherapy both directly and indirectly via stromal cell-derived aspartate.

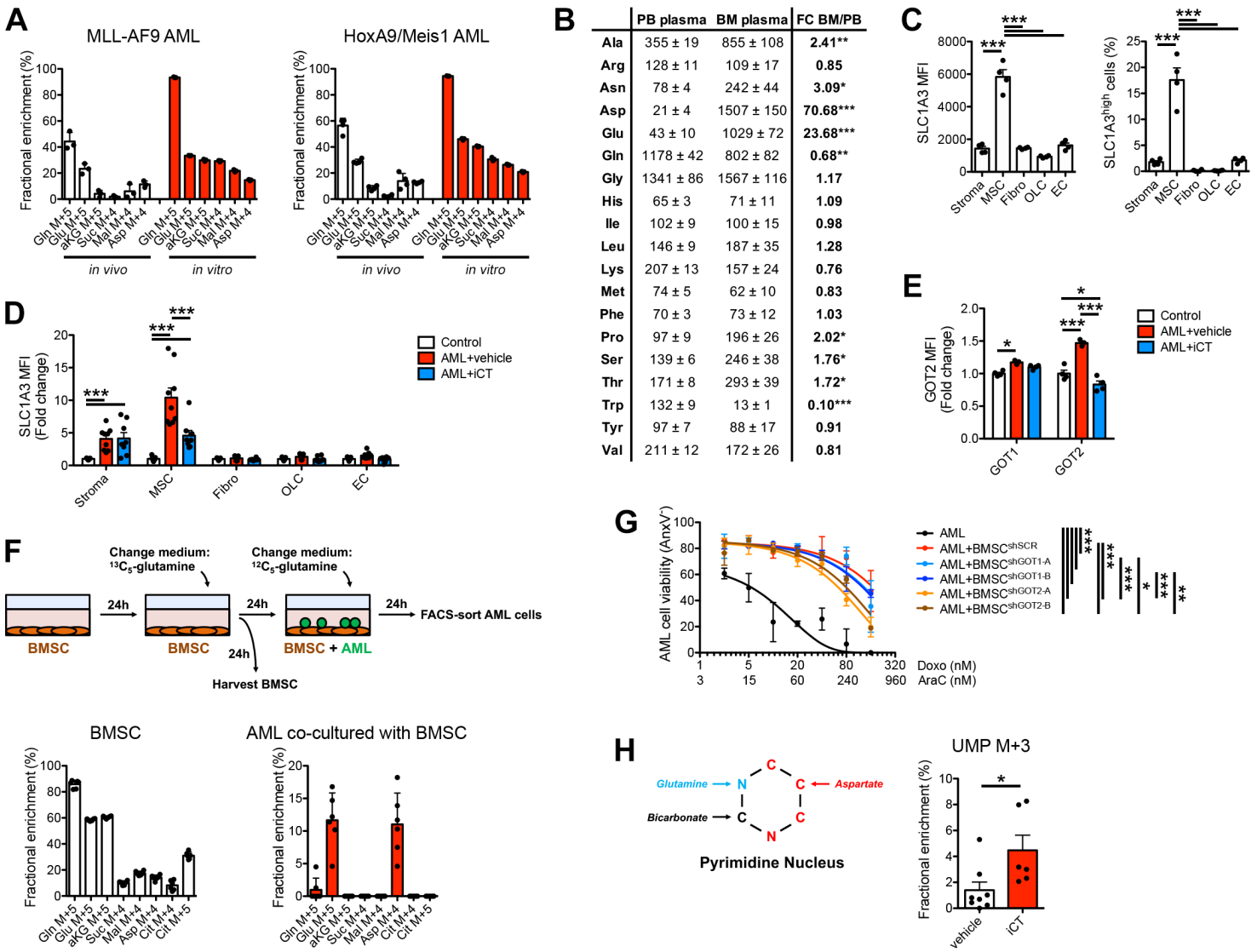

	PB plasma	BM plasma	FC BM/PB
Ala	355 ± 19	855 ± 108	2.41**
Arg	128 ± 11	109 ± 17	0.85
Asn	78 ± 4	242 ± 44	3.09*
Asp	21 ± 4	1507 ± 150	70.68***
Glu	43 ± 10	1029 ± 72	23.68***
Gln	1178 ± 42	802 ± 82	0.68**
Gly	1341 ± 86	1567 ± 116	1.17
His	65 ± 3	71 ± 11	1.09
Ile	102 ± 9	100 ± 15	0.98
Leu	146 ± 9	187 ± 35	1.28
Lys	207 ± 13	157 ± 24	0.76
Met	74 ± 5	62 ± 10	0.83
Phe	70 ± 3	73 ± 12	1.03
Pro	97 ± 9	196 ± 26	2.02*
Ser	139 ± 6	246 ± 38	1.76*
Thr	171 ± 8	293 ± 39	1.72*
Trp	132 ± 9	13 ± 1	0.10***
Tyr	97 ± 7	88 ± 17	0.91
Val	211 ± 12	172 ± 26	0.81

Figure 5. Bone Marrow Stromal Cell-Derived Aspartate Supports Pyrimidine Synthesis in AML Cells.

(**A**) Labeling of glutamine metabolism and TCA cycle metabolites in MLL-AF9 and HoxA9/Meis1 AML cells by $^{13}C_5$-glutamine *in vivo* and *in vitro* (10 minutes labeling). (**B**) LC-MS-based quantification of amino acid levels in PB and BM plasma of control mice. FC: fold change. (**C**) Flow cytometric analysis of SLC1A3 protein levels on the surface of different subpopulations of BMSC in control mice. Stroma: total stromal cells (CD45$^-$Ter119$^-$), MSC: mesenchymal stromal cells (CD45$^-$Ter119$^-$CD31$^-$LepR$^+$), Fibro: fibroblasts (CD45$^-$Ter119$^-$CD31$^-$LepR$^-$Sca1$^+$CD90$^+$), OLC: osteolineage cells: (CD45$^-$Ter119$^-$CD31$^-$LepR$^-$Sca1$^-$CD90^{low}CD105$^+$), EC: endothelial cells (CD45$^-$Ter119$^-$CD31$^+$CD105$^+$). Left: SLC1A3 mean fluorescence intensity (MFI), right: percentage SLC1A3^{high} cells. (**D**) Flow cytometric analysis of changes in SLC1A3 protein levels on the surface of BMSC subpopulations obtained from vehicle- or iCT-treated MLL-AF9 bearing mice at the moment of maximal response, compared to control mice. (**E**) Flow cytometric analysis of changes in intracellular GOT1 or GOT2 protein levels in MSCs obtained from vehicle- or iCT-treated MLL-AF9 bearing mice at the moment of maximal response, compared to control mice. (**F**) $^{13}C_5$-glutamine tracing in co-cultures of BMSC and MLL-AF9 AML cells showing transfer of glutamate and aspartate from BMSC to AML cells. (**G**) Viability of MLL-AF9 AML cells in mono-culture or co-

culture with BMSC transduced with shSCR, shGOT1 or shGOT2, in response to different doses of cytarabine (AraC) and doxorubicin (Doxo). (**H**) Labeling of UMP by $^{13}C_5$-glutamine in MLL-AF9 AML cells obtained from vehicle- or iCT-treated mice at the moment of maximal response. Data are represented as mean ± SEM. *p<0.05, **p<0.01, ***p<0.001. See also Figure S5.

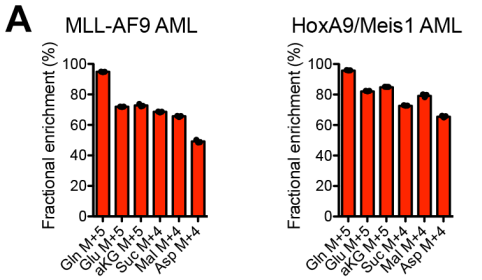

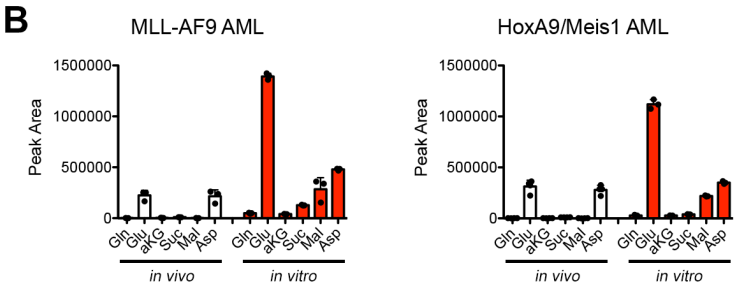

C

	Control		AML		AML+iCT	
	PB plasma	BM plasma	PB plasma	BM plasma	PB plasma	BM plasma
Ala	355 ± 19	855 ± 108	348 ± 26	1719 ± 166	413 ± 44	859 ± 180
Arg	128 ± 11	109 ± 17	100 ± 6	85 ± 3	120 ± 11	71 ± 6
Asn	78 ± 4	242 ± 44	69 ± 8	240 ± 19	81 ± 19	129 ± 14
Asp	21 ± 4	1507 ± 150	17 ± 2	2151 ± 231	11 ± 0	1049 ± 337
Glu	43 ± 10	1029 ± 72	44 ± 6	1775 ± 170	17 ± 4	782 ± 214
Gln	1178 ± 42	802 ± 82	1239 ± 42	450 ± 54	1182 ± 17	607 ± 68
Gly	1341 ± 86	1567 ± 116	1276 ± 31	1900 ± 111	1216 ± 23	1413 ± 143
His	65 ± 3	71 ± 11	59 ± 1	49 ± 2	70 ± 6	43 ± 4
Ile	102 ± 9	100 ± 15	103 ± 4	88 ± 5	88 ± 6	62 ± 4
Leu	146 ± 9	187 ± 35	152 ± 4	146 ± 12	132 ± 9	93 ± 5
Lys	207 ± 13	157 ± 24	178 ± 7	140 ± 8	197 ± 15	103 ± 4
Met	74 ± 5	62 ± 10	57 ± 6	47 ± 4	58 ± 5	37 ± 2
Phe	70 ± 3	73 ± 12	72 ± 2	56 ± 3	76 ± 11	44 ± 4
Pro	97 ± 9	196 ± 26	77 ± 7	245 ± 19	95 ± 14	160 ± 36
Ser	139 ± 6	246 ± 38	112 ± 4	154 ± 8	142 ± 21	145 ± 13
Thr	171 ± 8	293 ± 39	153 ± 8	385 ± 40	138 ± 17	171 ± 25
Trp	132 ± 9	13 ± 1	119 ± 7	8 ± 0	131 ± 31	15 ± 6
Tyr	97 ± 7	88 ± 17	82 ± 7	68 ± 4	89 ± 19	51 ± 5
Val	211 ± 12	172 ± 26	220 ± 3	152 ± 11	186 ± 16	110 ± 11

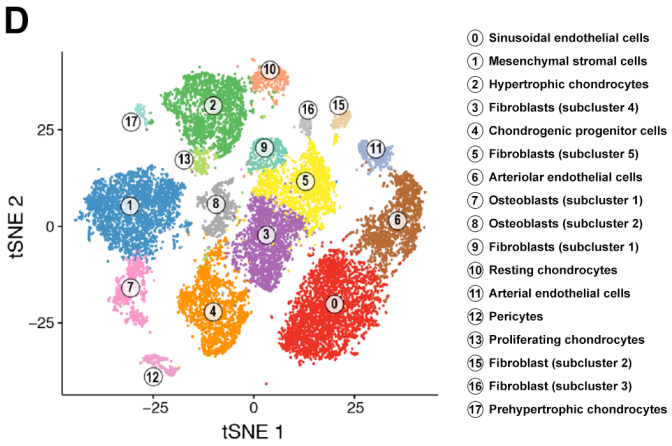

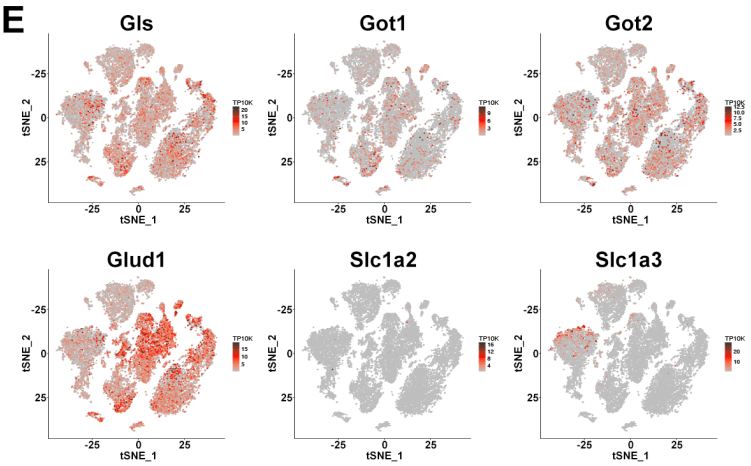

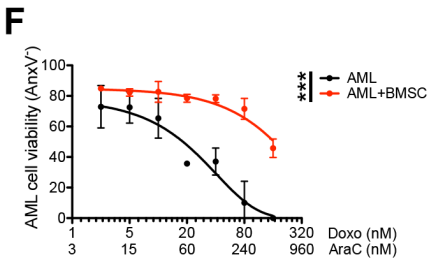

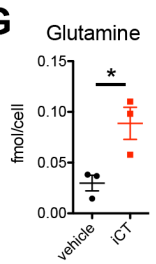

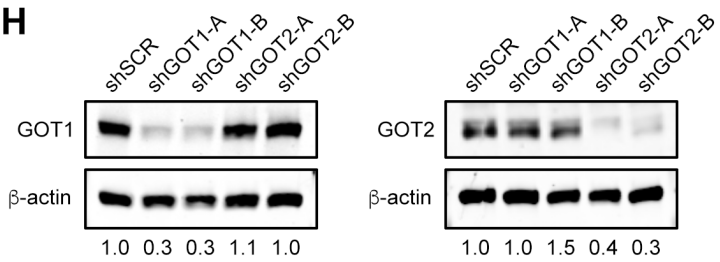

Figure S5. Bone Marrow Stromal Cell-Derived Aspartate Supports Pyrimidine Synthesis in AML Cells (related to Figure 5).

(**A**) Labeling of glutamine metabolism and TCA cycle metabolites in MLL-AF9 and HoxA9/Meis1 AML cells by $^{13}C_5$-glutamine *in vitro* (24 hours labeling). (**B**) LC-MS-based quantification of glutamine metabolism and TCA cycle metabolites in MLL-AF9 and HoxA9/Meis1 AML cells obtained from mice or from *in vitro* cell culture. (**C**) LC-MS-based quantification of amino acid levels in PB and BM plasma of control mice, MLL-AF9 AML-bearing mice and AML-bearing mice treated with iCT, at the moment of maximal response. (**D,E**) A cell atlas of the mouse bone marrow stroma obtained through single cell RNA sequencing. (D) t-SNE plot of 20,551 non-hematopoietic cells colored by clustering and annotated post hoc, showing 17 bone marrow stromal cell clusters. (E) t-SNE plots showing expression of *Gls*, *Got1*, *Got2*, *Glud1*, *Slc1a2* and *Slc1a3* in the mouse bone marrow stroma. (**F**) Viability of MLL-AF9 AML cells in mono-culture or co-culture with BMSC, in response to different doses of cytarabine (AraC) and doxorubicin (Doxo). (**G**) LC-MS-based quantification of glutamine in MLL-AF9 AML cells co-cultured with BMSC and treated with vehicle or with 30nM cytarabine and 10nM doxorubicin (iCT) for 24 hours. (**H**) Immunoblot detection of GOT1 and GOT2 in BMSC transduced with shSCR, shGOT1 or shGOT2, with β-actin as loading control. Data are represented as mean ± SEM. *p<0.05, ***p<0.001.

Discussion

Despite the clear clinical need to prevent or delay cancer relapse, it remains poorly understood how certain tumor cells manage to survive the extreme stress of chemotherapy. In the current study, we defined the metabolic profile of AML cells as they pass through that time of intense selection pressure. We found that residual AML cells exhibit transient metabolic adaptations driving their resistance to chemotherapy, and show in mouse models of AML that timed manipulation of specific metabolic pathways such as glutamine metabolism and pyrimidine synthesis holds therapeutic potential. These findings underscore the importance of cell metabolism as a primitive, first line stress protection mechanism that can be targeted to eliminate chemoresistant cancer cells.

To investigate the metabolic profile of AML cells at a time when the milieu of the bone marrow microenvironment is maximally hostile, we developed a pipeline for untargeted metabolomics of freshly-isolated AML cells from mice. While this approach provides a broad snapshot of cellular metabolism in an unbiased manner, it also bring several challenges. First, cell isolation, sorting and sample processing must be performed in a fast but standardized manner, limiting the time between animal euthanasia and metabolite extraction to minimize metabolic changes. We found that performing all steps at 4˚C greatly reduces procedural artefacts. Second, as with all metabolomics analyses, batch effects occur between individual experiments, but these seem to be even stronger when using low cell numbers. Including a reference sample that is taken along in each experiment helps significantly in correcting for this. Thirdly, and most importantly, data processing and analysis for untargeted metabolomics is highly labor-intensive. Inefficient peak alignment and limited MS/MS data, both more prominent due to the use of low cell numbers, requires substantial manual data processing and brings more uncertainty in metabolite identification. The use of both a reference sample and a pooled sample helps, especially with improving automatic metabolite annotation from cloud-based spectral databases. These approaches proved to be highly valuable in revealing the metabolic program of AML cells in their native environment, which would not have been obtained through transcriptomic analysis alone. In addition, a

key metabolic feature of residual cells, high glutamine levels, was lost once cells were isolated and cultured, and was also not observed when AML cells were treated with iCT *in vitro*. These results indicate that the dynamic metabolic adaptations of AML cells persisting after chemotherapy are regulated at the pathway activity level, and are highly dependent on the local microenvironment. This notion is further underscored by our metabolic tracer analysis, which revealed striking differences in glutamine metabolism in AML cells *in vitro* versus *in vivo*. The low contribution of glutamine to the TCA cycle in AML cells *in vivo* may explain the poor efficacy of GLS inhibition, even though this appears a promising target based on *in vitro* assays, and the peculiar nutritional composition of the bone marrow microenvironment with high glutamate levels may even further contribute to this lack of effect. The importance of examining the metabolism of cells in their native environment is supported by other recent studies that have shown that artificial *in vitro* conditions can create metabolic dependencies that do not exist *in vivo* (Cantor et al., 2017, Davidson et al., 2016, Muir et al., 2017).

Many studies have investigated the role of the bone marrow niche in AML progression and chemoresistance (Behrmann et al., 2018). However, most of these studies have focused on the role of adhesion molecules and cytokines. Very few studies have investigated the nutritional aspects of niche support in leukemia, with one report highlighting a role for bone marrow stromal cell-derived cysteine in chronic lymphocytic leukemia (Zhang et al., 2012), and a second study showing the importance of lipids provided by adipocytes for AML stem cells residing in adipose tissue (Ye et al., 2016). We now show that aspartate provided by $LepR^{+}$ stromal cells in the bone marrow can fuel nucleotide synthesis in AML cells, which becomes of particular importance in the setting of chemotherapy treatment. These findings again highlight the question of how much of chemoresistance development is determined by genetic alterations versus microenvironmental signals. Are there hotspots of aspartate production in the bone marrow that constitute a protective niche, and is there competition between AML subclones for occupancy of these aspartate-rich locations? The transgenic transplant-based mouse models used in the current study most likely do not possess the clonal complexity to answer this question. However, our documentation of the $SLC1A3^{high}$ subset of $LepR^{+}$ stromal cells may provide the means to identify

this putative chemoprotective niche in AML models that capture clonal evolution, such as transgenic mouse models with more mutational complexity (Heckl et al., 2014, Vassiliou et al., 2011), patient-derived xenografts (Potter et al., 2019, Wang et al., 2017), or even directly in patient samples. In addition, it will be of interest to examine whether this metabolic crosstalk with stromal cell subsets also plays a role in normal hematopoiesis, given that the bone marrow is unexpectedly rich in aspartate compared to peripheral blood (also true in control mice), and the known role of $LepR^{+}$ stromal cells in supporting hematopoietic stem cells (Ding et al. 2012b).

Translating our findings to clinical application may best be accomplished by exploiting the transient dependency on pyrimidine metabolism that we observed. It is currently not clear whether the basis for this dependency is nucleic acid polymer generation or other functions of UMP such as its role in *O*-linked *N*-acetylglycosylation (Bond and Hanover, 2015). In prior studies we defined that pyrimidine synthesis inhibition can induce differentiation of AML cells, indicating a broad range of effects in malignancy (Sykes et al., 2016). Notably, a number of pyrimidine synthesis inhibitors are now in clinical trial, including brequinar that we show here can remarkably extend animal survival when used for a brief interval post-chemotherapy. We suggest that our findings encourage testing of such inhibitors in a similar clinical context, given that the transient moment of stress that drives initial leukemia regeneration has also been described in AML patients (Boyd et al., 2018). We also suggest that this work justifies investigating our underlying hypothesis of a unique metabolic bottleneck associated with chemotherapy in the treatment of other tumor types.

Acknowledgments

The authors would like to thank Phillip Chea, Joyce LaVecchio and Nema Kheradmand for technical assistance, David Sykes for providing brequinar and help with experimental design, Scott Biller, Gillian Kingsbury, Shalini Sethumadavan and Donald Simons from Agios Pharmaceuticals for providing AGI15280 and help with experimental design, the HSCRB Histology Core for access to the cryostat, the HSCRB Flow Core for access to the flow cytometers, and the Harvard Center for Biological Imaging for access to the confocal microscope. N.v.G. was supported by a grant from Alex's Lemonade Stand Foundation and Tap Cancer Out. D.T.S. was supported by the Harvard Stem Cell Institute and the Ludwig Center at Harvard, as well as the Gerald and Darlene Jordan Chair of Medicine at Harvard University.

Author Contributions

N.v.G. initiated the project, designed, performed and analyzed experiments, and wrote the manuscript. J.B.S. performed and analyzed in vivo metabolic tracing experiments. Az.S. performed in vitro and in vivo experiments. Am.S. established the leukemia models. N.B. performed the single cell RNA sequencing. C.R. and T.O. performed the bulk RNA sequencing. E.G. and H.J.S. helped perform experiments. C.V. and S.A.T. designed and performed metabolomics and metabolite quantification experiments. M.C.H. contributed to the design and analysis of in vivo metabolic tracing experiments. D.T.S. initiated the project, analyzed data, provided supervision, and wrote the manuscript. All authors contributed to manuscript editing.

Declaration of Interests

D.T.S. is a director and equity holder of Agios Pharmaceuticals, Magenta Therapeutics, Editas Medicines, ClearCreekBio, Red Oak Medicines, and LifeVaultBio; he is a founder of Fate Therapeutics and Magenta Therapeutics and a consultant to FOG Pharma, VCanBio, and Bone Therapeutics. N.v.G., Am.S., T.O. and D.T.S. are inventors on patents related to this work.

STAR Methods

KEY RESOURCES TABLE

REAGENT or RESOURCE	SOURCE	IDENTIFIER
Antibodies		
Pacific Blue Lineage cocktail	BioLegend	Cat#: 133310 RRID: AB_11150779
APC anti-cKit	BioLegend	Cat#: 135108 RRID: AB_2028407
Brilliant Violet 510 anti-Sca1	BioLegend	Cat#: 108129 RRID: AB_2561593
eFluor 450 anti-CD34	eBioscience	Cat#: 48-0341-82 RRID: AB_2043837
PE-Cy7 anti-CD45	BioLegend	Cat#: 103114 RRID: AB_312979
PE-Cy7 anti-Ter-119	BioLegend	Cat#: 116222 RRID: AB_2281408
PerCP-Cy5.5 anti-CD31	BioLegend	Cat#: 102420 RRID: AB_10613644
APC anti-CD90.2	BioLegend	Cat#: 105312 RRID: AB_313183
Pacific Blue anti-CD105	BioLegend	Cat#: 120412 RRID: AB_2098890
Biotin anti-LepR	R&D Systems	Cat#: BAF497 RRID: AB_2296953
Anti-SLC1A3 (rabbit polyclonal)	Novus Biologicals	Cat#: NB100-1869 RRID: AB_531518
Anti-SLC38A1 (rabbit polyclonal)	ThermoFisher Scientific	Cat#: PA5-42420 RRID: AB_2605455
Alexa Fluor 647 anti-H2AX (pS139) (mouse monoclonal)	BD Biosciences	Cat#: 560447 RRID: AB_1645414
Anti-GOT1 (rabbit monoclonal)	Abcam	Cat#: ab170950
Anti-GOT2 (rabbit monoclonal)	Abcam	Cat#: ab171739
Anti-GLS (rabbit monoclonal)	ThermoFisher Scientific	Cat#: 701965 RRID: AB_2633041
Anti-β-actin (mouse monoclonal)	Sigma-Aldrich	Cat#: A2228 RRID: AB_476697
Alexa Fluor 546 anti-rabbit IgG (H+L)	ThermoFisher Scientific	Cat#: A11035 RRID: AB_2633041
IRDye 800CW anti-rabbit IgG (H + L)	LI-COR	Cat#: 925-32211 RRID: AB_2651127
IRDye 680RD anti-mouse IgG (H + L)	LI-COR	Cat#: 925-68070 RRID: AB_2651128
Chemicals, Peptides, and Recombinant Proteins		
Recombinant Mouse SCF Protein	R&D Systems	455-MC
Recombinant Mouse IL-3 Protein	R&D Systems	403-ML
Recombinant Mouse IL-6 Protein	R&D Systems	406-ML
D-luciferin	GoldBio	LUCK
Cytarabine hydrochloride	Sigma-Aldrich	C6645
Doxorubicin hydrochloride	Sigma-Aldrich	D1515

6-Diazo-5-oxo-L-norleucine (DON)	Sigma-Aldrich	D2141
(2-Hydroxypropyl)-β-cyclodextrin	Sigma-Aldrich	H107
Solutol HS 15	Sigma-Aldrich	42966
AGI15280	Agios Pharmaceuticals	N/A
Poly(ethylene glycol)-400	Sigma-Aldrich	202398
Brequinar (BRQ)	Broad Institute	N/A
7-aminoactinomycin D (7-AAD)	BD Biosciences	559925
BPTES	Sigma-Aldrich	SML0601
CB839	MedKoo Biosciences	206153
APC Annexin V	BioLegend	640941
APC-eFluor 780 Streptavidin	eBioscience	47-4317-82
CellROX Orange	ThermoFisher Scientific	C10443
Tetramethylrhodamine, Ethyl Ester (TMRE)	ThermoFisher Scientific	T669
RPMI 1640 Medium	Lonza	12-167F
DMEM Medium	Lonza	12-614F
Canonical Amino Acid Mix (^{13}C-, ^{15}N-labeled)	Cambridge Isotope Laboratories	MSK-CAA-1
L-Glutamine (13C5, 99%)	Cambridge Isotope Laboratories	CLM-1822-H
L-Glutamine (15N2, 98%)	Cambridge Isotope Laboratories	NLM-1328
Critical Commercial Assays		
BD Cytofix/Cytoperm Kit	BD Biosciences	554714
RNeasy Plus Mini Kit	Qiagen	74134
MethoCult GF M3434	StemCell Technologies	03434
Deposited Data		
RNA sequencing of MLL-AF9 leukemia cells sorted from mice treated with or without iCT, at the moment of maximal response or after relapse	GEO	GSE139159
Single cell RNA sequencing of mouse bone marrow stromal cells	GEO	GSE128423
Experimental Models: Cell Lines		
MLL-AF9 mouse AML	Sykes et al., 2016	N/A
HoxA9/Meis1 mouse AML	Sykes et al., 2016	N/A
Experimental Models: Organisms/Strains		
C57Bl/6J mice	Jackson Laboratories	000664
Recombinant DNA		
Mouse GLS shRNA (TRCN0000253167)	Sigma-Aldrich	SHCLND-NM_001081081
Mouse GOT1 shRNA (TRCN0000119792, TRCN0000119795)	Sigma-Aldrich	SHCLND-NM_010324
Mouse GOT2 shRNA (TRCN0000326018, TRCN0000326020)	Sigma-Aldrich	SHCLND-NM_010325
Software and Algorithms		
Compound Discoverer (version 3.0)	ThermoFisher Scientific	N/A
TraceFinder (version 4.1)	ThermoFisher Scientific	N/A
MassHunter (version B.08.00)	Agilent	N/A
MetaboAnalyst (version 4.0)	Chong et al., 2018	N/A

GSEA (version 4.0.2)	Mootha et al., 2003; Subramanian et al., 2005	N/A
Prism (version 5.0)	GraphPad Software	N/A
FlowJo (version 10)	FlowJo	N/A

Contact for Reagent and Resource Sharing

Further information and requests for reagents may be directed to, and will be fulfilled by, the corresponding author, David T. Scadden (david_scadden@harvard.edu).

Experimental Model and Subject Details

Mice

C57Bl/6J mice were purchased from Jackson Laboratories. Experiments were approved by the Institutional Animal Care and Use Committee (IACUC) of the Faculty of Arts and Sciences of Harvard University.

Syngeneic Leukemia Experiments

The MLL-AF9 and HoxA9/Meis1 leukemia models have been described previously (Sykes et al., 2016). Briefly, the MLL-AF9 model was established by crossing MLL-AF9 knockin mice (Corral et al., 1996) with mice expressing GFP under the control of the ubiquitin promoter as well as mice expressing luciferase under the control of the β-actin promoter. The retroviral transduction model of HoxA9/Meis1 leukemia was generated by the infection of bone marrow mononuclear cells with an MSCV-HoxA9-IRES-Meis1 construct (originally designed by Dr. Guy Sauvageau). For both models, leukemic bone marrow cells from a terminally ill mouse were harvested and expanded *ex vivo* in RPMI1640 medium (Lonza) supplemented with 10% fetal bovine serum (FBS; Gibco), 100 I.U./ml penicillin, 100 µg/ml streptomycin, 2 mM L-glutamine (all from Corning), 20 ng/ml recombinant mouse SCF (rmSCF), 10 ng/ml recombinant mouse interleukin 3 (rmIL-3) and 10 ng/ml rmIL-6 (all from R&D Systems).

Recipient male mice (age 8-10 weeks) were injected intravenously (retro-orbital) with 1 million leukemia cells in a volume of 100 µl of saline. Disease progression was tracked intravitally using bioluminescence imaging. Mice were anaesthetized using isoflurane, injected with luciferin (150 µl of a 15 mg/ml solution in PBS), and imaged on an IVIS 200 Spectrum In Vivo Imaging System (PerkinElmer). When indicated, mice were treated with iCT (cytarabine, 100 mg/kg, once daily for 5 days and doxorubicin, 3 mg/kg, once daily for the first 3 days) or vehicle (saline) delivered via I.P. injection. To inhibit glutamine metabolism, mice were treated with DON (0.3 mg/kg, once daily) or vehicle (saline) delivered via I.P. injection. To inhibit GLS, mice were treated with AGI15280 (150 mg/kg, twice daily) or vehicle (20% HP-β-cyclodextrin + 20% Solutol, 50 mM citrate buffer, pH 3) delivered by oral gavage. To inhibit DHODH, mice were treated with BRQ (50 mg/kg, once daily) or vehicle (70% PBS, 30% poly(ethylene glycol)-400, pH 7.2) delivered via I.P. injection. To inhibit GCL, mice were treated with BSO (twice daily by I.P. injection at 2.23 mg/kg + in the drinking water at 4.45 mg/ml) or vehicle (saline by I.P. injection + untreated drinking water). For survival experiments, mice were checked twice daily and euthanized by CO_2 asphyxiation when they showed signs of extensive distress or became moribund.

Method Details

Cell Isolation and Culture

The MLL-AF9 or HoxA9/Meis1 primary leukemia cells were expanded in RPMI1640 medium supplemented with 10% FBS, 100 I.U./ml penicillin, 100 µg/ml streptomycin, 2 mM L-glutamine, 20 ng/ml rmSCF, 10 ng/ml rmIL-3 and 10 ng/ml rmIL-6. Leukemia cells were cultured in a humidified incubator at 37˚C in ambient air with 5% CO_2.

For BMSC, femurs and tibias of mice were isolated and cleaned to remove muscle. Epiphyses were cut away and bone marrow was flushed out with PBS containing 2% FBS using a 25 gauge needle attached to a 20 ml syringe. Bone marrow fractions were kept on ice. Bones were cut into small pieces using scissors and digested in DMEM medium (Lonza) containing 3 mg/ml collagenase type 2 (Gibco) and 4 mg/ml dispase (Gibco) at 37˚C for 45 minutes. Bone cell suspensions were then pooled with the bone

marrow fraction and passed through a 70 µm cell strainer. Cells were used for immediate analysis or cultured in DMEM medium supplemented with 20% FBS, 100 I.U./ml penicillin, 100 µg/ml streptomycin and 2 mM L-glutamine, in a humidified incubator at 37˚C in 2% O_2 with 7.5% CO_2.

For co-cultures, BMSC were seeded in 96-well plates at 15,000 cells/well and AML cells were added at 5,000 cells/well. Cells were cultured in DMEM medium supplemented with 20% dialyzed FBS (Gibco), 100 I.U./ml penicillin, 100 µg/ml streptomycin, 0.4 mM L-glutamine, 20 ng/ml rmSCF, 10 ng/ml rmIL-3 and 10 ng/ml rmIL-6, in a humidified incubator at 37˚C in 2% O_2 with 7.5% CO_2.

Isolation of Peripheral Blood and Bone Marrow Plasma

Mice were euthanized by CO_2 asphyxiation and peripheral blood was obtained by cardiac puncture and collected in K2-EDTA Microtainer tubes (BD Biosciences). Peripheral blood plasma was obtained by centrifuging samples for 5 minutes at 2,500 x g. Femurs and tibias were dissected, cleaned and epiphyses cut off. Bone marrow plasma was obtained by centrifugation for 5 minutes at 2,500 x g.

Fluorescence-activated Cell Sorting (FACS)

Mice were euthanized by CO_2 asphyxiation and femurs and tibias were isolated and cleaned to remove muscle. Bones were then crushed using a mortar and pestle in ice-cold flow buffer (PBS containing 2% FBS), and the obtained cell suspension was passed through a 70 µm cell strainer. Red blood cells were removed by incubating cells for 5 minutes in ACK lysing buffer (Gibco) on ice, cells were washed and resuspended in ice-cold flow buffer containing the viability dye 7-aminoactinomycin D (7-AAD; BD Biosciences). Viable AML cells ($GFP^+7\text{-}AAD^-$) were sorted on a BD FACSAria II (BD Biosciences) with the sample collector cooled to 4˚C. Sorted cells were immediately processed.

Flow Cytometry

Cells were suspended in flow buffer and stained for 30 minutes at 4°C in the dark with antibodies against cKit, Sca1, CD34, CD45, Ter-119, CD31, LepR, CD90, CD105, SLC1A3, SLC38A1 or a lineage cocktail

(CD3, Gr-1, CD11b, B220, Ter-119). 7-AAD was included as a viability dye to help identify dead cells. When necessary, cells were stained with a secondary antibody (Alexa Fluor 546-conjugated anti-rabbit IgG) or APC-eFluor 780-conjugated streptavidin (eBioscience) for 15 minutes at 4°C in the dark. For intracellular antibody staining cells were first stained for surface markers and then fixed and permeabilized (BD Cytofix/Cytoperm Kit, BD Biosciences). Samples were then stained with antibodies against GOT1, GOT2 or gamma H2AX in perm/wash buffer, washed and, for GOT1 and GOT2, stained with a secondary antibody (Alexa Fluor 546-conjugated anti-rabbit IgG). Cell viability was analyzed using Annexin V-APC (BioLegend) and propidium iodide (PI; ThermoFisher Scientific) with Annexin V^- PI^- cells considered as viable cells. The number of viable cells was determined by taking into account the total number of cells per well as measured using a Cellometer (Nexcelom). Mitochondrial membrane potential was measured by Tetramethylrhodamine, ethyl ester (TMRE; ThermoFisher) staining and levels of ROS were measured by CellROX Orange staining. Cells were incubated with 200 nM TMRE or 2.5 µM CellROX Orange in RPMI1640 medium supplemented with 10% FBS, 100 I.U./ml penicillin, 100 µg/ml streptomycin and 2 mM L-glutamine at 37˚C for 30 minutes, washed in flow buffer and analyzed. For all flow cytometry experiments, single color controls were used to set compensations and fluorescence minus one controls were used to set gates. All flow cytometry data was collected on a BD LSR II flow cytometer and analyzed using FlowJo software.

Colony-forming unit assay

FACS-sorted viable AML cells ($GFP^+7\text{-}AAD^-$) were resuspended in MethoCult GF M3434 (StemCell Technologies) at 1000 cells/ml and plated in SmartDish 6-well plates (StemCell Technologies) at 1 ml/well in duplicate. Cells were cultured in a humidified incubator at 37˚C in ambient air with 5% CO_2. After 5 days colonies were counted.

Metabolomics Analysis

FACS-sorted cells or plasma samples were lysed in ice-cold methanol and polar metabolites were extracted using methanol-chloroform phase separation (methanol:water:chloroform in 2:1:2 ratio).

Samples were then dried under nitrogen flow, resuspended in 70% acetonitrile in water containing 2.5 µM of an internal standard (^{13}C-, ^{15}N-labeled amino acid mix; Cambridge Isotope Laboratories) and run on a ThermoFisher Q-exactive equipped with Zic-pHILIC column (150x2.1 mm, 5 µm; Merck). A volume of 5 µl was injected and the full mass spectrum was obtained in both positive and negative mode (0 to 45 minutes, resolution 70000, AGC target 3e6, m/z range 66 to 990). Mobile phase A for chromatography consisted of 20 mM ammonium carbonate, 0.1% ammonium hydroxide, in water and mobile phase B of 97% acetonitrile in water. For untargeted metabolomics, a pooled sample was created from all samples and used for MS/MS runs. For targeted analysis, a standard mix at 1 µM of each compound of interest was prepared and run after the samples to confirm retention times.

For untargeted metabolomics analysis, data were processed with Compound Discoverer 3.0 (ThermoFisher Scientific) using the mzCloud mass spectral library for compound annotation. For compounds for which an MS/MS spectrum was not available, the Kyoto Encyclopedia of Genes and Genomes (KEGG) Compound database (www.genome.jp/kegg; Kanehisa and Goto, 2000) and human metabolome database (HMDB; www.hmdb.ca; Wishart et al., 2007, Wishart et al., 2019) were used for putative compound annotation based on the monoisotopic molecular weight. For targeted metabolomics analysis, data were analyzed with Tracefinder4.1 (ThermoFisher Scientific).

In Vitro Metabolic Tracing

Cells in culture were incubated with 2 mM $^{13}C_5$-glutamine (Cambridge Isotope Laboratories) in glutamine-free media for the indicated times and harvested by centrifugation at 4˚C. An aliquot of each well was taken at the time of harvesting to determine cell numbers. After washing with PBS, cells were lysed in ice-cold methanol and polar metabolites were extracted using methanol-chloroform phase separation (methanol:water:chloroform in 2:1:2 ratio). Samples were then dried under nitrogen flow, resuspended in 70% acetonitrile in water containing 2.5 µM of an internal standard (^{13}C-, ^{15}N-labeled amino acid mix) and run on a ThermoFisher Q-exactive equipped with Zic-pHILIC column (150x2.1 mm, 5 µm; Merck). A volume of 5 µl was injected and the full mass spectrum was obtained in both positive

and negative polarity mode (0 to 45 minutes, resolution 70000, AGC target 3e6, m/z range 66 to 990). Mobile phase A for chromatography consisted of 20 mM ammonium carbonate, 0.1% ammonium hydroxide, in water and mobile phase B of 97% acetonitrile in water. A standard mix at 5 µM of each compound of interest was prepared and run after the samples to confirm retention times and to obtain the experimental value of natural isotopic distribution. Data were analyzed with Tracefinder 4.1. Each compound peak was integrated as the sum of all isotopes. The isotope ratios were then extracted from the mass spectral data.

***In Vivo* Metabolic Tracing**

Mice were injected via the tail vein with 200 µl of a 54.3 mg/ml $^{13}C_5$-glutamine or $^{15}N_2$-glutamine (Cambridge Isotope Laboratories) in saline solution. At the indicated times after injection, mice were euthanized by CO_2 asphyxiation and femurs and tibias were isolated and processed for FACS. FACS-sorted cells were lysed in ice-cold 80% methanol in water. Samples were dried down using a SpeedVac Vacuum Concentrator (ThermoFisher) and re-suspended in mobile phase buffer A (97% H_2O, 3% MeOH, 10 mM Tributylamine, 15 mM Glacial Acetic Acid, pH 5.5). Metabolites were analyzed on a reverse phase ion-pairing chromatography (ZORBAX Extend-C18, 2.1 × 150 mm, 1.8 µm; Agilent) coupled to tandem mass spectrometry (Agilent), and analytes were eluted in buffer A and buffer B (10 mM Tributylamine, 15 mM Glacial Acetic Acid in 100% MeOH). Samples were ionized (with negative polarity) using Agilent Jet Spray ionization; nebulizer 45 psi, capillary –2000 V, nozzle voltage: 500 V, sheath gas temperature 325 °C, and sheath gas flow 12 L/min. Peaks were integrated in Mass Hunter (Agilent).

RNA sequencing

Total RNA was isolated using the RNeasy Plus Mini kit (Qiagen), with additional on-column DNase treatment to eliminate traces of genomic DNA. Nucleic acid concentration was quantified using a NanoDrop (Thermo Scientific). Libraries were prepared with an RNA library preparation kit (E7490, NEB) using 100 ng of RNA. RNA-seq libraries were sequenced with a 1 X 50-bp strand-specific protocol

on a HiSeq 2500 (Illumina). Data were analyzed using a high-throughput next generation sequencing analysis pipeline: FASTQ files were aligned to the mouse genome (mm9) and gene expression profile for the individual samples was calculated for RPKM values using STAR and Cufflinks.

Single cell RNA sequencing

The single cell RNA sequencing dataset of the mouse long bone and bone marrow stroma was generated previously and detailed information on cell isolation, cell sorting, library preparation, RNA sequencing and data processing is provided in the original manuscript (Baryawno et al. 2019).

Immunoblotting

Total cell lysates were obtained by lysing equal amounts of cells in RIPA buffer (ThermoFisher Scientific) supplemented with 1x cOmplete protease inhibitor cocktail (Roche). Proteins were separated by SDS-PAGE and transferred to a nitrocellulose membrane (Bio-Rad). Membranes were blocked with 5% dry milk in Tris-buffered saline with 0.1% Tween-20 (TBS-T) for 1 hour at room temperature and incubated overnight at 4°C with primary antibodies (rabbit-anti-GLS, 1/1,000; rabbit-anti-GOT1, 1/1000; rabbit-anti-GOT2, 1/1000; mouse-anti-β-actin, 1/10,000) diluted in 5% BSA (Cell Signaling Technology) in TBS-T. Signals were detected using an Odyssey CLx imaging system (LI-COR) after incubation with IRDye-conjugated secondary antibodies (LI-COR).

shRNAs

To silence GLS, GOT1 and/or GOT2 we transduced cells, in the presence of 7 μg/ml polybrene (Sigma-Aldrich), with a lentivirus carrying a shRNA against mouse GLS (MISSION, Sigma-Aldrich; TRCN0000253167), mouse GOT1 (MISSION, Sigma-Aldrich; TRCN0000119792, TRCN0000119795) and/or mouse GOT2 (MISSION, Sigma-Aldrich; TRCN0000326018, TRCN0000326020). A nonsense scrambled (SCR) shRNA sequence was used as a negative control. Cells were transduced by spinfection (90 minutes at 1,000 x g), incubated for 3 hours, washed and plated in fresh medium.

Histology

Bones were harvested, fixed overnight in 4% paraformaldehyde in PBS and decalcified using 10% EDTA (pH 8). Bones were then embedded in gelatin-polyvinylpyrrolidone-sucrose and sectioned on a cryostat (50 µm sections) according to a previously published protocol (Kusumbe et al., 2015). Cell nuclei were visualized by Hoechst33342 (ThermoFisher Scientific) and mounted. Images were taken on a Zeiss LSM880 confocal laser scanning microscope.

Statistical Analysis

Analysis of the untargeted metabolomics dataset was performed using MetaboAnalyst (www.metaboanalyst.ca; Chong et al., 2018). The “Statistical Analysis” and “Pathway Analysis” nodes were used for analysis. Data was normalized by log transformation (generalized logarithm transformation) and auto-scaling (mean-centered and divided by the standard deviation of each variable). For pathway analysis, the Global Test and Relative-betweenness Centrality algorithms were used, and data were mapped to the mouse KEGG pathway library.

Gene set enrichment analysis was performed using the Gene Set Enrichment Analysis (GSEA) software (Broad Institute; Mootha et al., 2003, Subramanian et al., 2005) using the hallmark and GO biological process gene sets.

Correlation between AML patient survival and gene expression was performed using the PROGgeneV2 prognostics database (Goswami and Nakshatri, 2014). The GSE12417 and TCGA datasets were used for analysis.

All numerical results are reported as mean ± standard error of the mean (s.e.m.). Statistical significance of the difference between experimental groups was analyzed by two-tailed unpaired Student’s t-test, one-way ANOVA with Bonferroni post-hoc test or the log-rank (Mantel-Cox) test for the survival curve

analyses using the GraphPad PRISM 5 software. Differences were considered statistically significant for $P < 0.05$.

Data and Software Availability

The bulk mRNA sequencing data that support the findings of this study have been deposited in GEO with the accession number GSE139159. The single cell RNA sequencing data were generated previously (Baryawno et al. 2019) and are deposited in GEO (GSE128423). A portal for exploring the entire single cell atlas is available (portals.broadinstitute.org/single_cell/study/mouse-bone-marrow-stroma-in-homeostasis). All other data supporting the findings of this study are available within the paper.

Supplemental Tables

Table S1. Untargeted Metabolomics Analysis of Residual AML Cells. Related to Figures 1, S1.

Table S2. Statistical Analysis of Untargeted Metabolomics Data. Related to Figures 1, S1.

References

1. Baryawno, N., Przybylski, D., Kowalczyk, M.S., Kfoury, Y., Severe, N., Gustafsson, K., Kokkaliaris, K.D., Mercier, F., Tabaka, M., Hofree, M., et al. (2019). A cellular taxonomy of the bone marrow stroma in homeostasis and leukemia. Cell *177*, 1915-1932.
2. Behrmann, L., Wellbrock, J., and Fiedler, W. (2018). Acute myeloid leukemia and the bone marrow niche - take a closer look. Front. Oncol. *8*, 444.
3. Bond, M.R., and Hanover, J.A. (2015). A little sugar goes a long way: the cell biology of O-GlcNAc. J. Cell Biol. *208*, 869-880.
4. Boyd, A.L., Aslostovar, L., Reid, J., Ye, W., Tanasijevic, B., Porras, D.P., Shapovalova, Z., Almakadi, M., Foley, R., Leber, B., et al. (2018). Identification of chemotherapy-induced leukemic-regenerating cells reveals a transient vulnerability of human AML recurrence. Cancer Cell *34*, 483-498.
5. Cantor, J.R., Abu-Remaileh, M., Kanarek, N., Freinkman, E., Gao, X., Louissaint, A., Jr., Lewis, C.A., and Sabatini, D.M. (2017). Physiologic medium rewires cellular metabolism and reveals uric acid as an endogenous inhibitor of UMP synthase. Cell *169*, 258-272.
6. Chen, W.L., Wang, Y.Y., Zhao, A., Xia, L., Xie, G., Su, M., Zhao, L., Liu, J., Qu, C., Wei, R., et al. (2016). Enhanced fructose utilization mediated by SLC2A5 is a unique metabolic feature of acute myeloid leukemia with therapeutic potential. Cancer Cell *30*, 779-791.
7. Chong, J., Soufan, O., Li, C., Caraus, I., Li, S., Bourque, G., Wishart, D.S., and Xia, J. (2018). MetaboAnalyst 4.0: towards more transparent and integrative metabolomics analysis. Nucleic Acids Res. *46*, W486-W494.
8. Corral, J., Lavenir, I., Impey, H., Warren, A.J., Forster, A., Larson, T.A., Bell, S., McKenzie, A.N., King, G., and Rabbitts, T.H. (1996). An Mll-AF9 fusion gene made by homologous recombination causes acute leukemia in chimeric mice: a method to create fusion oncogenes. Cell *85*, 853-861.

9. Davidson, S.M., Papagiannakopoulos, T., Olenchock, B.A., Heyman, J.E., Keibler, M.A., Luengo, A., Bauer, M.R., Jha, A.K., O'Brien, J.P., Pierce, K.A., et al. (2016). Environment impacts the metabolic dependencies of Ras-driven non-small cell lung cancer. Cell Metab. *23*, 517-528.
10. Dietmair, S., Timmins, N.E., Gray, P.P., Nielsen, L.K., and Krömer, J.O. (2010). Towards quantitative metabolomics of mammalian cells: development of a metabolite extraction protocol. Anal. Biochem. *404*, 155-164.
11. Ding, L., Ley, T.J., Larson, D.E., Miller, C.A., Koboldt, D.C., Welch, J.S., Ritchey, J.K., Young, M.A., Lamprecht, T., McLellan, M.D., et al. (2012a). Clonal evolution in relapsed acute myeloid leukaemia revealed by whole-genome sequencing. Nature *481*, 506-510.
12. Ding, L., Saunders, T.L., Enikolopov, G., and Morrison, S.J. (2012b). Endothelial and perivascular cells maintain haematopoietic stem cells. Nature *481*, 457-62.
13. Farge, T., Saland, E., de Toni, F., Aroua, N., Hosseini, M., Perry, R., Bosc, C., Sugita, M., Stuani, L., Fraisse, M., et al. (2017). Chemotherapy-resistant human acute myeloid leukemia cells are not enriched for leukemic stem cells but require oxidative metabolism. Cancer Discov. *7*, 716-735.
14. German, N.J., Yoon, H., Yusuf, R.Z., Murphy, J.P., Finley, L.W., Laurent, G., Haas, W., Satterstrom, F.K., Guarnerio, J., Zaganjor, E., et al. (2016). PHD3 loss in cancer enables metabolic reliance on fatty acid oxidation via deactivation of ACC2. Mol. Cell *63*, 1006-1020.
15. Gregory, M.A., Nemkov, T., Park, H.J., Zaberezhnyy, V., Gehrke, S., Adane, B., Jordan, C.T., Hansen, K.C., D'Alessandro, A., and DeGregori, J. (2019). Targeting glutamine metabolism and redox state for leukemia therapy. Clin. Cancer Res. *25*, 4079-4090.
16. Häussinger, D., and Schliess, F. (2007). Glutamine metabolism and signaling in the liver. Front. Biosci. *12*, 371-391.
17. Heckl, D., Kowalczyk, M.S., Yudovich, D., Belizaire, R., Puram, R.V., McConkey, M.E., Thielke, A., Aster, J.C., Regev, A., and Ebert, B.L. (2014). Generation of mouse models of myeloid

malignancy with combinatorial genetic lesions using CRISPR-Cas9 genome editing. Nat. Biotechnol. *32*, 941-946.

18. Jacque, N., Ronchetti, A.M., Larrue, C., Meunier, G., Birsen, R., Willems, L., Saland, E., Decroocq, J., Maciel, T.T., Lambert, M., et al. (2015). Targeting glutaminolysis has antileukemic activity in acute myeloid leukemia and synergizes with BCL-2 inhibition. Blood *126*, 1346-1356.
19. Kanehisa, M., and Goto, S. (2000). KEGG: Kyoto Encyclopedia of Genes and Genomes. Nucleic Acids Res. *28*, 27-30.
20. Keller, M.A., Kampjut, D., Harrison, S.A., and Ralser, M. (2017). Sulfate radicals enable a non-enzymatic Krebs cycle precursor. Nat. Ecol. Evol. *1*, 83.
21. Krivtsov, A.V., Twomey, D., Feng, Z., Stubbs, M.C., Wang, Y., Faber, J., Levine, J.E., Wang, J., Hahn, W.C., Gilliland, D.G., et al. (2006). Transformation from committed progenitor to leukaemia stem cell initiated by MLL-AF9. Nature *442*, 818-822.
22. Kültz, D. (2005). Molecular and evolutionary basis of the cellular stress response. Annu. Rev. Physiol. *67*, 225-257.
23. Kusumbe, A.P., Ramasamy, S.K., Starsichova, A., and Adams, R.H. (2015). Sample preparation for high-resolution 3D confocal imaging of mouse skeletal tissue. Nat. Protoc. *10*, 1904-1914.
24. Lagadinou, E.D., Sach, A., Callahan, K., Rossi, R.M., Neering, S.J., Minhajuddin, M., Ashton, J.M., Pei, S., Grose, V., O'Dwyer, K.M., et al. (2013). BCL-2 inhibition targets oxidative phosphorylation and selectively eradicates quiescent human leukemia stem cells. Cell Stem Cell *12*, 329-341.
25. Lemberg, K.M., Vornov, J.J., Rais, R., and Slusher, B.S. (2018). We're not "DON" yet: optimal dosing and prodrug delivery of 6-diazo-5-oxo-L-norleucine. Mol. Cancer Ther. *17*, 1824-1832.
26. Magee, J.A. (2017). Comment on: Genomics of primary chemoresistance and remission induction failure in paediatric and adult acute myeloid leukaemia. Br. J. Haematol. *176*, 5-6.
27. Matre, P., Velez, J., Jacamo, R., Qi, Y., Su, X., Cai, T., Chan, S.M., Lodi, A., Sweeney, S.R., Ma, H., et al. (2016). Inhibiting glutaminase in acute myeloid leukemia: metabolic dependency of selected AML subtypes. Oncotarget *7*, 79722-79735.

28. Mootha, V.K., Lindgren, C.M., Eriksson, K.F., Subramanian, A., Sihag, S., Lehar, J., Puigserver, P., Carlsson, E., Ridderstråle, M., Laurila, E., et al. (2003). PGC-1alpha-responsive genes involved in oxidative phosphorylation are coordinately downregulated in human diabetes. Nat. Genet. *34*, 267-273.
29. Muir, A., Danai, L.V., Gui, D.Y., Waingarten, C.Y., Lewis, C.A., and Vander Heiden, M.G. (2017). Environmental cystine drives glutamine anaplerosis and sensitizes cancer cells to glutaminase inhibition. Elife *6*, e27713.
30. Naviaux, R.K. (2014). Metabolic features of the cell danger response. Mitochondrion *16*, 7-17.
31. Ni, F., Yu, W.M., Li, Z., Graham, D.K., Jin, L., Kang, S., Rossi, M.R., Li, S., Broxmeyer, H.E., and Qu, C.K. (2019). Critical role of ASCT2-mediated amino acid metabolism in promoting leukaemia development and progression. Nat. Metab. *1*, 390-403.
32. Nowell, P.C. (1976). The clonal evolution of tumor cell populations. Science *194*, 23-28.
33. Pei, S., Minhajuddin, M., Callahan, K.P., Balys, M., Ashton, J.M., Neering, S.J., Lagadinou, E.D., Corbett, C., Ye, H., Liesveld, J.L., et al. (2013). Targeting aberrant glutathione metabolism to eradicate human acute myelogenous leukemia cells. J. Biol. Chem. *288*, 33542-33558.
34. Potter, N., Miraki-Moud, F., Ermini, L., Titley, I., Vijayaraghavan, G., Papaemmanuil, E., Campbell, P., Gribben, J., Taussig, D., and Greaves, M. (2019). Single cell analysis of clonal architecture in acute myeloid leukaemia. Leukemia *33*, 1113-1123.
35. Subramanian, A., Tamayo, P., Mootha, V.K., Mukherjee, S., Ebert, B.L., Gillette, M.A., Paulovich, A., Pomeroy, S.L., Golub, T.R., Lander, E.S., et al. (2005). Gene set enrichment analysis: a knowledge-based approach for interpreting genome-wide expression profiles. Proc. Natl. Acad. Sci. USA *102*, 15545-15550.
36. Sykes, D.B., Kfoury, Y.S., Mercier, F.E., Wawer, M.J., Law, J.M., Haynes, M.K., Lewis, T.A., Schajnovitz, A., Jain, E., Lee, D., et al. (2016). Inhibition of dihydroorotate dehydrogenase overcomes differentiation blockade in acute myeloid leukemia. Cell *167*, 171-186.
37. Tardito, S., Oudin, A., Ahmed, S.U., Fack, F., Keunen, O., Zheng, L., Miletic, H., Sakariassen, P.Ø., Weinstock, A., Wagner, A., et al. (2015). Glutamine synthetase activity fuels nucleotide

biosynthesis and supports growth of glutamine-restricted glioblastoma. Nat. Cell Biol. *17*, 1556-1568.

38. Vassiliou, G.S., Cooper, J.L., Rad, R., Li, J., Rice, S., Uren, A., Rad, L., Ellis, P., Andrews, R., Banerjee, R., et al. (2011). Mutant nucleophosmin and cooperating pathways drive leukemia initiation and progression in mice. Nat. Genet. *43*, 470-475.
39. Wang, K., Sanchez-Martin, M., Wang, X., Knapp, K.M., Koche, R., Vu, L., Nahas, M.K., He, J., Hadler, M., Stein, E.M., et al. (2017). Patient-derived xenotransplants can recapitulate the genetic driver landscape of acute leukemias. Leukemia *31*, 151-158.
40. Wang, Y.H., Israelsen, W.J., Lee, D., Yu, V.W.C., Jeanson, N.T., Clish, C.B., Cantley, L.C., Vander Heiden, M.G., and Scadden, D.T. (2014). Cell-state-specific metabolic dependency in hematopoiesis and leukemogenesis. Cell *158*, 1309-1323.
41. Wishart, D.S., Tzur, D., Knox, C., Eisner, R., Guo, A.C., Young, N., Cheng, D., Jewell, K., Arndt, D., Sawhney, S., et al. (2007). HMDB: the Human Metabolome Database. Nucleic Acids Res. *35*, D521-D526.
42. Wishart, D.S., Feunang, Y.D., Marcu, A., Guo, A.C., Liang, K., Vázquez-Fresno, R., Sajed, T., Johnson, D., Li, C., Karu, N., et al. (2018). HMDB 4.0: the human metabolome database for 2018. Nucleic Acids Res. *46*, D608-D617.
43. Ye, H., Adane, B., Khan, N., Sullivan, T., Minhajuddin, M., Gasparetto, M., Stevens, B., Pei, S., Balys, M., Ashton, J.M., et al. (2016). Leukemic stem cells evade chemotherapy by metabolic adaptation to an adipose tissue niche. Cell Stem Cell *19*, 23-37.
44. Zhang, W., Trachootham, D., Liu, J., Chen, G., Pelicano, H., Garcia-Prieto, C., Lu, W., Burger, J.A., Croce, C.M., Plunkett, W., et al. (2012). Stromal control of cystine metabolism promotes cancer cell survival in chronic lymphocytic leukaemia. Nat. Cell Biol. *14*, 276-286.